WILEY-VCH

High-Efficiency Perovskite Solar Cells using Molecularly-Engineered, Thiophene-Rich, Hole-Transporting Materials: Influence of Alkyl Chain Length on Power Conversion Efficiency

Iwan Zimmermann,[†] Javier Urieta-Mora,[†] Paul Gratia, Juan Aragó, Giulia Grancini, Agustín Molina-Ontoria,* Enrique Ortí,* Nazario Martín,* Mohammad Khaja Nazeeruddin*

This work is dedicated to the memory of Harold W. Kroto

Dr. I. Zimmermann, P. Gratia, Dr. Giulia Grancini and Prof. M. K. Nazeeruddin
Group for Molecular Engineering of Functional Materials
and Laboratory for Photonics and Interfaces
EPFL VALAIS, CH-1951 Sion, Switzerland
E-mail: mdkhaja.nazeeruddin@epfl.ch

J. Urieta-Mora, Dr. A. Molina-Ontoria, Prof. N. Martín
IMDEA-Nanociencia
C/ Faraday 9, Ciudad Universitaria de Cantoblanco
28049 Madrid, Spain
E-mail: nazmar@ucm.es

J. Urieta-Mora, Prof. N. Martín.
Departamento Química Orgánica, Facultad C. C. Químicas
Universidad Complutense de Madrid
Av. Complutense s/n, 28040 Madrid (Spain)
Homepage: http://www.ucm.es/info/fullerene/

Dr. J. Aragó, Prof. E. Ortí
Instituto de Ciencia Molecular
Universidad de Valencia
Catedrático José Beltrán 2, 46980, Paterna (Spain)

[†] These authors contributed equally to this work.

The synthesis and characterization of a series of novel small-molecule hole-transporting materials (HTMs) based on an anthra[1,2-b:4,3-b′:5,6-b″:8,7-b‴]tetrathiophene (ATT) core are reported. The new compounds follow an easy synthetic route and have no need of expensive purification steps. The novel HTMs were tested in perovskite solar cells (PSCs) and power conversion efficiencies (PCE) of up to 18.1 % under 1 sun irradiation were

measured. This value is comparable with the 17.8 % efficiency obtained using *spiro*-OMeTAD as a reference compound. Similarly, a significant quenching of the Photoluminescence in the first nanosecond is observed, indicative of effective hole transfer. Additionally, the influence of introducing aliphatic alkyl chains acting as solubilizers on the device performance of the ATT molecules is investigated. Replacing the methoxy groups on the triarylamine sites by butoxy-, hexoxy- or decoxy-substituents greatly improved the solubility of the compounds without changing the energy levels, yet at the same time significantly decreasing the conductivity as well as the PCE, 17.3 % for ATT-OBu, 15.7 % for ATT-OHex and 9.7 % for ATT-ODec.

1. Introduction

The publication of methylammonium lead iodide ($CH_3NH_3PbI_3$) as a light-absorbing material in solution-based solar cells by Miyasaka and col. in 2009 has unleashed a scientific run in the development of perovskite photovoltaics.[1] Simple device architectures, the ability to solution-process the organic-inorganic hybrid perovskite material and good power conversion efficiencies have made of perovskite solar cells (PSCs) the new rising star in thin film photovoltaics.[2,3] Organic-inorganic hybrid perovskites show excellent optoelectronic properties such as good light absorption,[4, 5] long electron and hole diffusion lengths[6, 7] and high charge-carrier mobilities.[8] Furthermore, the perovskite material is highly versatile, and its properties can be widely tuned by anionic and cationic substitution. Engineering of the perovskite material and the charge extracting layers have led to rapid improvement in power conversion efficiencies from initial 3.8 % to over 22 % today, certified by NREL.[9] Replacing methylammonium with the slightly larger formamidinium cation has shown to lower the band gap of the perovskite material, extending the light that can be absorbed further into the infrared region,[10] whereas replacing iodine by bromide widens the band gap yet at the same time enhancing the charge carrier lifetime in the perovskite. The best device efficiencies

reported in the literature have been obtained by modifying the composition of the perovskite. Seok and col.[11] used a combination of two perovskite materials with the nominal formula [FAPbI$_3$]$_{0.85}$[MAPbBr$_3$]$_{0.15}$ (FA = formamidinium, MA = methylammonium). Our group employed a triple cation perovskite (Cs, FA and MA) with the generic form Cs$_x$(MA$_{0.17}$FA$_{0.83}$)$_{(100-x)}$Pb(I$_{0.83}$Br$_{0.17}$)$_3$, which results in a thermally more stable and versatile perovskite achieving efficiencies higher than 21 %.[12]

Whereas great advances in engineering of the perovskite materials have been made, the development of more efficient, stable and cheaper hole-transporting materials (HTMs) is lagging behind. The field is indeed dominated by the HTM 2,2′,7,7′-tetrakis(*N,N*-di-*p*-methoxyphenylamine)-9,9′-*spiro*bifluorene (*spiro*-OMeTAD) and by the even more expensive poly[bis(4-phenyl)-(2,4,6-trimethylphenyl)amine] (PTAA).[13, 14] Developing new HTM molecules through inexpensive synthetic routes and without needing of tedious purification steps remains therefore as a primary goal. Finding HTMs that exhibit hole-injection and transport properties similar to *spiro*-OMeTAD and PTAA, and closely match the valence band edge of the perovskite is the key for avoiding any loss in electrical potential and charge recombination. Although simple inorganic HTMs such as CuSCN[15, 16] or CuI[17] have been proposed, the efficiencies achieved remain low compared to those obtained with the state-of-the-art PTAA polymer or *spiro*-OMeTAD small molecule.

The most common structures of the HTMs for PSCs are based on simple molecules decorated with arylamines and/or diarylamine-substituted carbazoles, which exhibit excellent hole-injection and transport properties via radical cation species.[18-26] An alternative chemical approach for designing high efficient HTMs is based on polycyclic aromatics as a central core, such as pentacene,[27] triazatruxene,[28] thiolated nanographene[29] or benzotrithiophene,[30] endowed with arylamines derivatives. These π-conjugated structures show excellent hole-transporting properties due to the stacking of the planar structure through intramolecular π–π interactions, which lead to excellent power conversion efficiencies. Recently, the introduction

3

of thiophene units within the conjugated core of the HTM molecules has shown to enhance the sulfur-iodine interaction with the perovskite layer leading to more efficient hole extraction.[31]

Combining these features, here we report the design, synthesis, characterization and photovoltaic performance of a new family of easily attainable HTMs based on an anthra[1,2-b:4,3-b′:5,6-b″:8,7-b‴]tetrathiophene (ATT) core endowed with *p*-alkoxytriphenylamines of different alkyl chain length. ATT is a sulfur-rich polycyclic aromatic hydrocarbon with a flat and rigid π conjugated structure, which consists on four thiophene units fused to an anthracene (Scheme 1). It is well-known that this structure tends to stack through strong π–π interactions and leads to excellent hole-carrier mobilities in organic field-effect transistors (OFETs).[32, 33] The star-shaped ATT molecules are obtained following a simple synthetic route with high yields and show excellent PCE values over 18 % when used in PSC devices. The influence of alkyl chains often introduced to increase the solubility of the HTM molecule is furthermore investigated. Although longer aliphatic side chains do not influence the electronic energy levels, they have a significant influence on the conductivity of the material and thereby on the device performance.

2. Results and Discussion

The synthetic pathway towards the preparation of the new HTMs is illustrated in **Scheme 1** and experimental details are given in the Supporting Information (SI). The ATT central core was prepared following a well-established procedure, which involves a four-fold Stille cross coupling between commercially available 1,2,4,5-tetrabromobenzene and 2-(tributylstannyl)thiophene, followed by a bromination employing N-bromosuccinimide (NBS), giving rise to the tetrabrominated derivative **3**. The FeCl₃-mediated Scholl reaction of compound **3** leads to the formation of the π-extended derivative **4**. The tetrabromo derivative **4** was obtained in almost 80 % overall yield (three synthetic steps) and, more importantly, no further purification (column chromatography) was required for any of the synthetic steps.

Finally, *p*-alkoxytriphenylamines were covalently linked to the central core **4** by a four-fold Suzuki cross coupling in moderate to good yields, ranging from 46 % to 72 %.

Complete structural characterization of the new HTMs was undertaking using analytical and spectroscopic techniques such as ^{1}H and ^{13}C NMR, FTIR and mass spectrometry. The ^{1}H and ^{13}C NMR spectra reveal the expected resonance signals of the aliphatic and aromatic protons and carbons.

ATT-OMe R = CH_3 (72 %)
ATT-OBu R = C_4H_9 (61 %)
ATT-OHex R = C_6H_{13} (53 %)
ATT-ODec R = $C_{10}H_{21}$ (46 %)
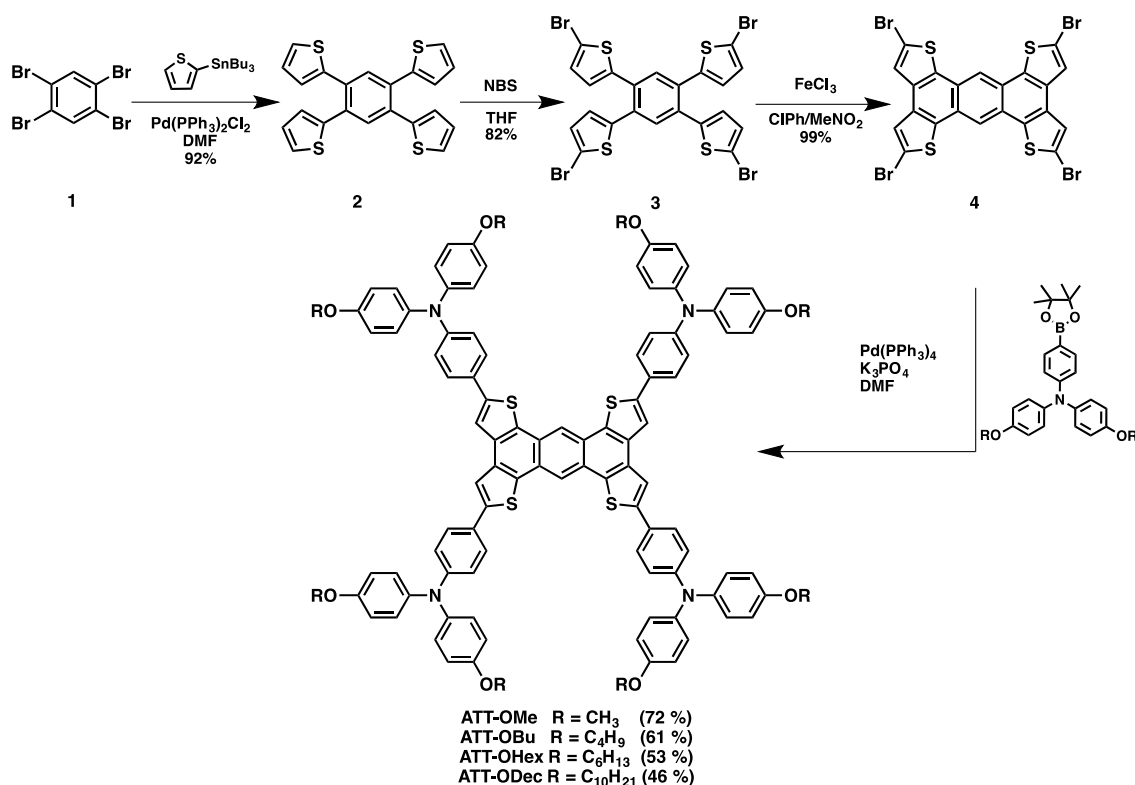
Scheme 1. Synthetic route for the preparation of the star-shaped hole-transporting materials ATT-OMe, ATT-OBu, ATT-OHex and ATT-ODec.

The electrochemical properties of the ATT derivatives were studied by cyclic voltammetry (**Figure 1**a) in argon-purged CH_2Cl_2 solutions at a scan rate of 100 mV s^{-1}, and the redox potentials are summarized in **Table 1**. The new HTMs are only active in the anodic scan, where two consecutive reversible oxidation waves are observed. The ATT derivatives show very similar half-wave oxidation potentials and the value estimated for the first oxidation potential is 0.88 V *vs.* normal hydrogen electrode (NHE). Using this value, the energy derived for the highest-occupied molecular orbital (HOMO) of the ATT derivatives is −5.32 eV,

which is slightly lower than that of *spiro*-OMeTAD (–5.16 eV) estimated under similar conditions.[21] Therefore, the new derivatives exhibit an excellent band-alignment between the HOMO of the HTM and the valence band edge of the perovskite (see below). Thus, an efficient hole injection from the HTM to the perovskite is expected. It is worth noting that there is no significant variation in the HOMO energy by increasing the length of the alkyl chain.

Table 1. Electrochemical and optical properties of ATT derivatives and *spiro*-OMeTAD.

HTM	$E^{ox}_{1/2}$ [V][a]	E_{HOMO} [eV][b]	$\lambda_{max, abs}$ [nm][c]	$\lambda_{max, em}$ [nm][c]	E^{0-0}[eV][d]	E_{LUMO} [eV][e]
ATT-OMe	0.88	–5.32	402	549	2.49	–2.82
ATT-OBu	0.88	–5.32	402	554	2.49	–2.83
ATT-OHex	0.87	–5.31	402	554	2.49	–2.82
ATT-ODec	0.88	–5.32	402	554	2.49	–2.83
Spiro-OMeTAD	0.72	–5.16	386	319	3.05	–2.11

[a] Determined from CV measurements *vs.* normal hydrogen electrode (NHE). [b] E_{HOMO} is estimated in eV by $E_{HOMO} = -4.44$ eV $- E^{ox}_{1/2}$. [c] λ_{max} of absorption and emission were measured in CH_2Cl_2 solutions. [d] E^{0-0} was determined at the intersection of normalized absorption and emission spectra. [e] E_{LUMO} were estimated by $E_{LUMO} = E_{HOMO} + E^{0-0}$.

To gain more insight into the electron-donor properties of the ATT derivatives, quantum chemical calculations were performed at the B3LYP/6-31G** level for ATT-OMe, its constituting fragments (the ATT core and the *p*-methoxytriphenylamine (OMeTPA) unit) and the *spiro*-OMeTAD compound as a reference compound (see the SI for computational details). Note that the electronic properties hardly change with the length of the alkyl chain and, thus, only the ATT-OMe system was computed as a representative ATT derivative.

Figure 1b shows the frontier molecular orbitals calculated for the ATT core, the OMeTPA addends and the ATT-OMe and *spiro*-OMeTAD HTMs. The HOMO of ATT-OMe clearly corresponds to the HOMO of the ATT core with significant contributions from the neighboring phenyl rings and nitrogen atoms of the OMeTPA groups, whereas the lowest-unoccupied molecular orbital (LUMO) fully resides on the ATT core. It is important to note that the HOMO is strongly destabilized in passing from ATT (−5.30 eV) to ATT-OMe (−4.45

eV) as a consequence of the antibonding interaction between the HOMOs of the constituting ATT and OMeTPA moieties (**Figure 1**b). This destabilization largely enhances the electron-donor character of ATT-OMe compared to the ATT core and determines that the HOMO of ATT-OMe approaches that of *spiro*-OMeTAD (**Figure 1**b). The HOMO of ATT-OMe is indeed predicted 0.29 eV lower in energy than the HOMO of the archetypical *spiro*-OMeTAD HTM (−4.16 eV) in good agreement with the slightly higher oxidation potential measured for the former (0.88 vs 0.72 V, Table 1). The difference between the theoretical values predicted for the energy of the HOMO and those obtained experimentally (Table 1) is that the former are computed for the isolated molecules in gas phase whereas the latter are estimated from the oxidation potentials measured in solution.
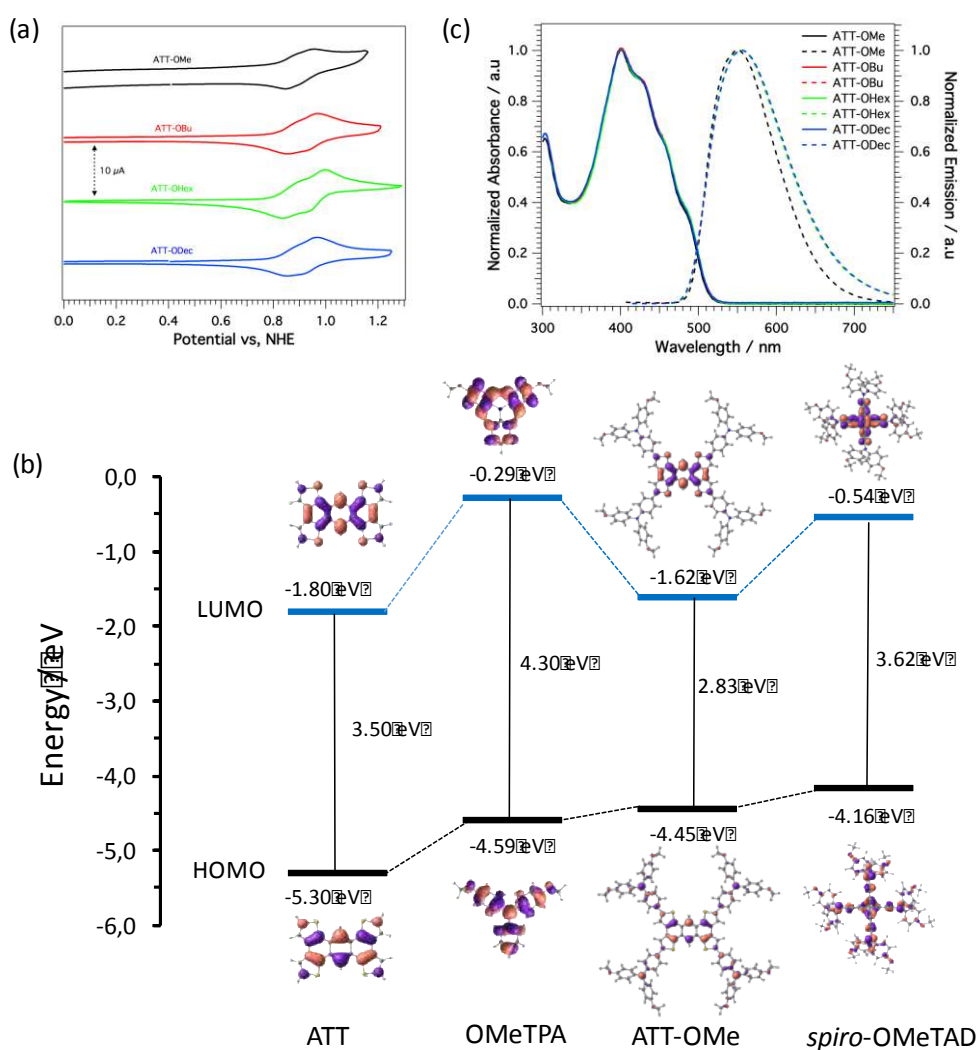
Figure 1. (a) Cyclic voltammograms of ATT derivatives in $TBAPF_6/CH_2Cl_2$ at a scan rate of 100 mV s^{-1}. (b) Energy diagram showing the frontier molecular orbitals computed for ATT, OMeTPA, ATT-OMe and *spiro*-OMeTAD compounds at the B3LYP/6-31G** level. (c) UV-Visible (solid line) and fluorescence emission spectra (dashed line) of ATT derivatives in CH_2Cl_2. All samples were measured at ambient temperature.

Hole reorganization energies (λ) were also calculated at the B3LYP/6-31G** level to evaluate the ability of the ATT derivatives as HTMs (see the SI for computational details). The λ values computed for the ATT core, the OMeTPA groups and the ATT-OMe and *spiro*-OMeTAD compounds are 0.126, 0.274, 0.096 and 0.139 eV, respectively. The ATT-OMe compound therefore exhibits a very small λ value, significantly smaller than the reorganization energy calculated for the ATT core (see the SI for further explanation) and for the reference *spiro*-OMeTAD compound. The small λ value obtained for ATT-OMe is indeed comparable to the reorganization energies found for the best organic *p*-type semiconducting materials (e.g., oligoacenes or heteroacenes).[34, 35] These findings clearly highlight the potential of ATT-OMe as a hole-transporting material for PSC devices with a good electronic level alignment (similar to *spiro*-OMeTAD) and a small reorganization energy that facilitates the charge transport in the material.

The optical properties of the ATT-based HTMs were studied using absorption and emission spectroscopy (**Figure 1**c), and the recorded absorption and emission wavelengths are collected in **Table 1.** In CH_2Cl_2 solution, the ATT compounds exhibit a strong absorption band in the 300–500 nm range, with a maximum centered at 402 nm ($\varepsilon = 1.5 \times 10^{-5}$ M cm^{-1}). Thus, the limited absorption of these HTMs in the visible region will not interfere in the generated photocurrent due to the strong absorption of the perovskite. B3LYP/6-31G** calculations of the singlet excited electronic states (S_n) ascribe this band to the intense electronic transitions $S_0 \rightarrow S_1$, $S_0 \rightarrow S_2$, $S_0 \rightarrow S_3$ and $S_0 \rightarrow S_6$ calculated at 498, 495, 458 and 440 nm, respectively (Table S1). These electronic transitions are of $\pi \rightarrow \pi^*$ nature and imply one-electron excitations from the HOMO and HOMO–1 to the LUMO and LUMO+1 which are, all of them, mainly located on the ATT core (Figure S3.3).

The emission spectra exhibit a maximum centered at 554 nm for ATT-OBu, ATT-OHex and ATT-ODec, whereas the emission of ATT-OMe is slightly blue-shifted, with a maximum at 549 nm. The large separation between the absorption and emission maxima (~ 150 nm) observed for all the ATT derivatives is attributed to the participation of different singlet excited states in the absorption, the transition to the lowest-energy S_1 being predicted at 2.49 eV (498 nm). The optical band gap (E_{0-0}) estimated from the absorption and emission intersection is indeed of 2.50 eV for all of the HTMs. It is important to note that no significant change in the absorption and emission spectra was observed when increasing the length of the alkyl chains.
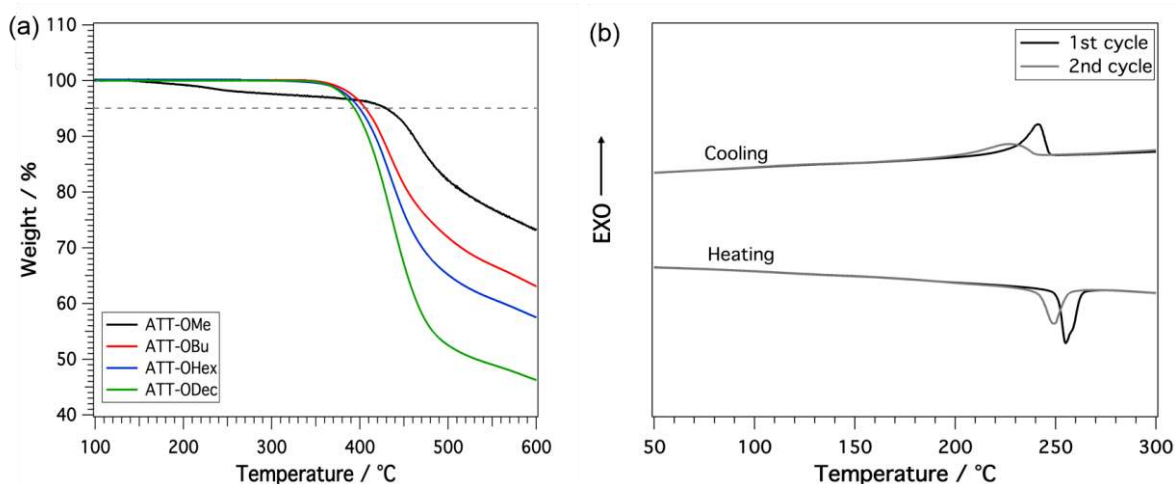
Figure 2. (a) Thermogravimetric analysis curves recorded for ATT-based HTMs under nitrogen at 10 °C min^{-1} of heating rate. (b) Differential scanning calorimetry of ATT-OMe under nitrogen at heating rate of 20 °C min^{-1} (1st and 2nd cycle).

Relevant insights into the thermal properties of the new HTMs were provided by thermogravimetric analysis (TGA) and differential scanning calorimetry (DSC). Detailed thermal features are collected in **Table 2**. ATT derivatives exhibit good thermal stability and start decomposing at temperatures (T_{dec}) above 390 °C (5% weight loss under N_2 atmosphere) as shown in **Figure 2**a. As expected, the thermal stability increases when shortening the length of the alkyl chains. Inspecting the DSC of ATT-OMe during the first scan reveals a crystalline behavior with a melting temperature (T_m) of 254 °C and a cooling crystallization temperature (T_{cr}) of 242 °C, which are still observed after consecutive heating/cooling cycles

(**Figure 2**b). ATT-OBu and ATT-OHex present a melting temperature of 284 and 206 °C and a glass transition (T_g) temperature of 131 and 95 °C, respectively, which suggest a crystalline and an amorphous nature for ATT-OBu and ATT-OHex, respectively. Finally, ATT-ODec exhibits four consecutive phase transitions with a T_g at 60 °C obtained from the second cycle, which indicates its amorphous nature.

Table 2. Thermal properties of ATT derivatives

	T_{dec} [°C][a]	T_m [°C][b]	T_g [°C][b]	T_{cr} [°C][b]
ATT-OMe	430	254	-	242
ATT-OBu	405	284	131	-
ATT-OHex	398	206	95	-
ATT-ODec	393	58, 82, 124, 158	60[c]	-

[a] Decomposition temperature determined from TGA (5% weight loss under N_2 atmosphere). [b] Determined from the first cycle of the DSC under nitrogen atmosphere. [c] Determined for the second cycle of the DSC under nitrogen atmosphere
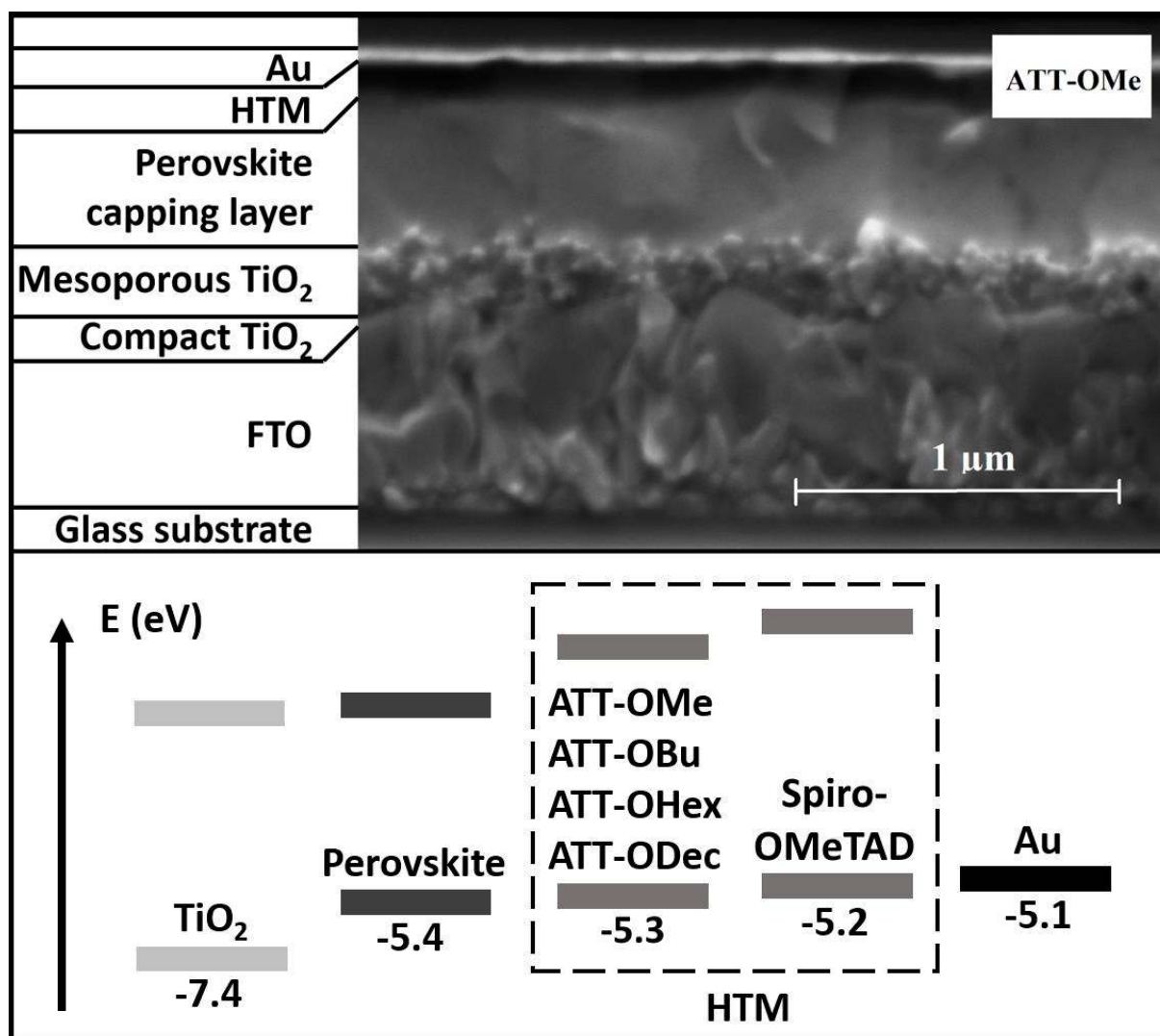
Figure 3. Cross-section SEM picture showing the different layers of a PSC device (top), and the energy diagram of the different components of the PSC (bottom).

The new small-molecule ATT derivatives were tested as HTMs in solution-processed PSC devices. The devices were prepared from a stack of thin layers onto fluorine-doped tin oxide (FTO) coated glass that serves as the backbone. The different layers can be seen from the schematic illustration and the cross-section scanning electron microscopy (SEM) image displayed in **Figure 3**. The layers forming the PSC device are: ~30 nm compact TiO_2 serving as blocking layer, ~200 nm mesoporous TiO_2 filled with perovskite, ~400 nm perovskite capping layer, HTM layer, and ~80 nm thermally evaporated gold for the electrodes. The photoactive perovskite material is a mixed-anion/mixed-cation compositional modification based on the nominal formula $[FAPbI_3]_{0.85}[MAPbI_3]_{0.15}$ with around 5 % of lead-iodide excess.

11

This particular perovskite derivative has been chosen due to its superior performances compared to simple MAPbI$_3$.[36] The perovskite layer was fabricated by spin-coating a precursor solution containing PbI$_2$, PbBr$_2$, FAI and MAI in stoichiometric amounts dissolved in DMF:DMSO 4:1. During the spin-coating process, a small amount of chlorobenzene was poured onto the spinning substrate to obtain a smooth, shiny perovskite layer after annealing for 45 min at 100 °C. The HTMs were applied by spin-coating a chlorobenzene solution containing cobalt dopant (FK209), Li-TFSI and tert-butylpyridine as additives. Detailed procedure of the device fabrication is given in the SI.

Due to the poor solubility of ATT-OMe at room temperature, this molecule was applied by heating the HTM solution as well as the substrate to 100 °C; at this temperature ATT-OMe is completely solubilized for a concentration of 20 mM. This procedure made possible to get very smooth and uniform layers of around 150 nm thicknesses. The long alkyl chains on the remaining ATT derivatives increased the solubility remarkably, and 30 mM HTM concentrations spin-coated at room temperature resulted in similar thicknesses. Although good solubility is usually key for obtaining uniform HTM layers with thicknesses greater than 100 nm, we observed that the film quality became worse going for longer alkyl chains, especially for ATT-OHex and ATT-ODec. The roughness of those HTM layers can also be observed from the SEM images.
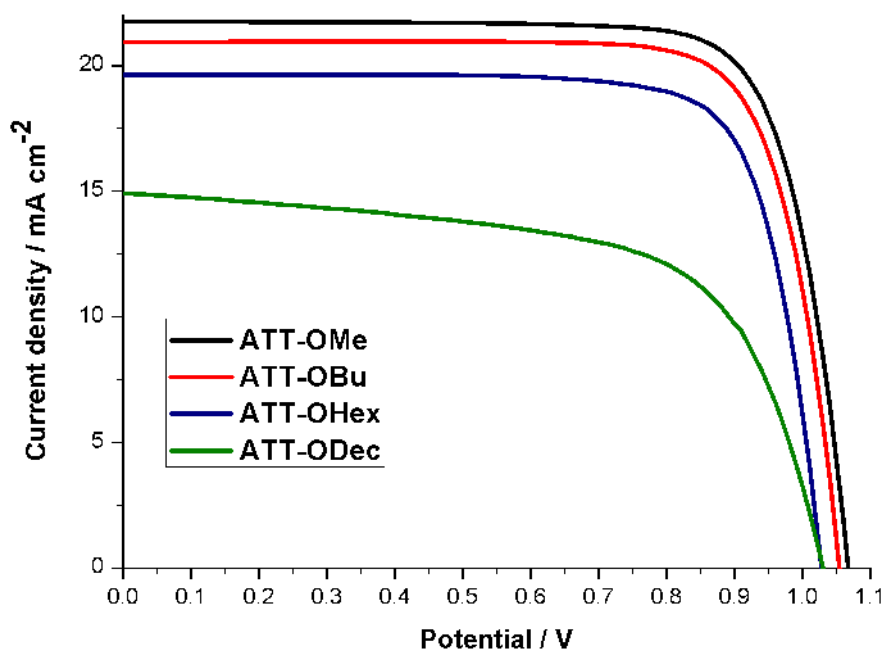
Figure 4. Current density-voltage graph comparing the different ATT derivatives. The curves were recorded using a scan speed of 20 mV s^{-1}.

Table 3. Device performance of the ATT derivatives compared to *spiro*-OMeTAD.

	V_{oc} [V]	J_{sc} [mA cm^{-2}]	Fill Factor [%]	*PCE* [%]
ATT-OMe	1070	21.75	78.1	18.13
ATT-OBu	1050	20.94	78.3	17.28
ATT-OHex	1030	19.60	77.8	15.66
ATT-ODec	1030	14.92	62.9	9.67
Spiro-OMeTAD	1120	21.33	74.4	17.80

The performance of the PSC devices employing the different ATT molecules and *spiro*-OMeTAD as a reference was measured under 1 sun 1.5 AMG (100 mW cm^{-2}) irradiation. Current-voltage scans were recorded sweeping from open circuit voltage (V_{oc}) towards 0 V at 20 mV s^{-1}. Full hysteresis scans are given in the SI. The $J-V$ graphs are shown in **Figure 4** and the results are summarized in **Table 3**. ATT-OMe shows the highest performance, with a power conversion efficiency (*PCE*) over 18.1 %, similar to the *spiro*-OMeTAD reference. Upon increasing the length of the peripheral alkyl chains, the device efficiency decreases to

17.28 % for ATT-OBu, 15.66 % for ATT-OHex and 9.67 % for ATT-ODec. For the ATT derivatives with longer alkyl chains, the short circuit current (J_{sc}) decreases significantly from 21.75 mA cm^{-2} for ATT-OMe to 14.92 mA cm^{-2} for ATT-ODec. The theoretical J_{sc} values integrated from the external quantum efficiencies (EQEs) are consistent with those experimentally observed in all cases (Figure S5.1.1).
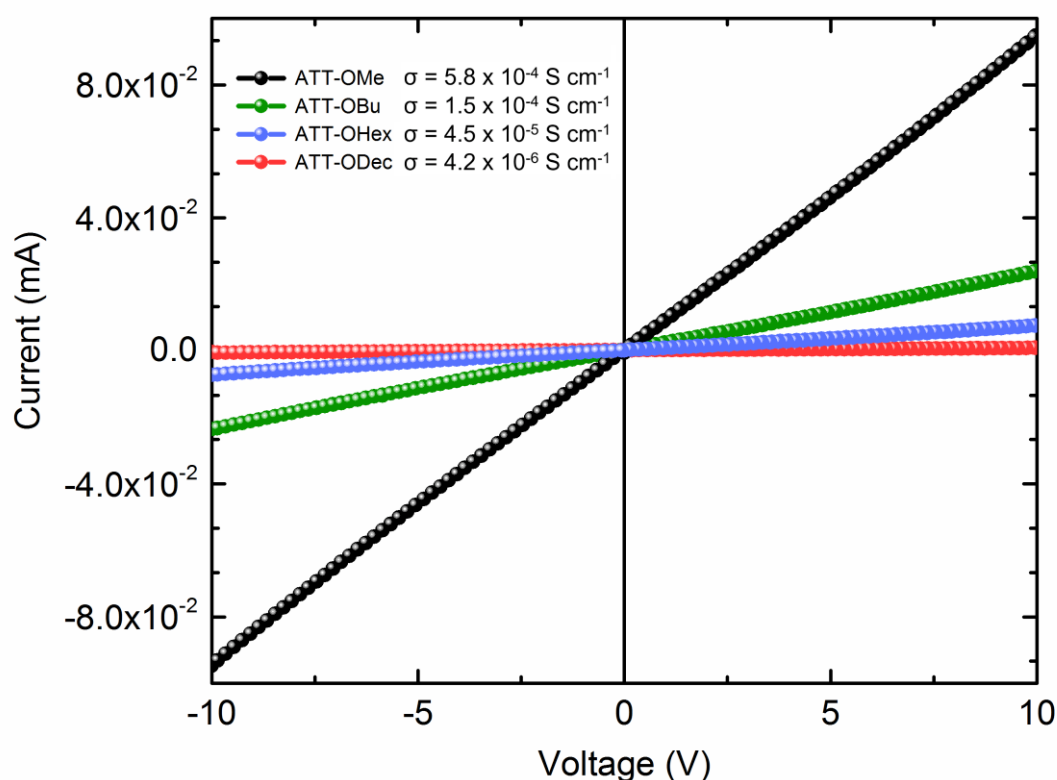

Figure 5. Conductivity of the ATT derivatives measured on substrates having interdigitating gold electrodes with a channel length of 2.5 μm. The conductivity within the HTM film is gradually reduced with longer alkyl chain substituents.

To further investigate the observed trend in solar cell performance we measured the conductivity of the different ATT molecules. HTM solutions doped with 6% FK209 were spin-coated onto a substrate having interdigitating gold electrodes with a channel length of 2.5 μm. $I-V$ scans between −10 and +10 V were recorded, and the conductivity of the different molecules was calculated using Ohm's law. Semi-logarithmic conductivity plots are shown in **Figure 5** as well as the corresponding calculated conductivity values. Remarkable

14

conductivity was observed for ATT-OMe (5.8×10^{-4} S cm^{-1}), which is even higher than that previously measured for *spiro*-OMeTAD (8.7×10^{-5} S cm^{-1}).[25] Upon increasing the length of the alkyl chains the conductivity decreases gradually, and for ATT-ODec the conductivity value was found to be two orders of magnitude lower than for ATT-OMe. These findings are in good agreement with the device performance. Efficient HTMs need to have high electrical conductivity to guarantee efficient current collection. We speculate that longer alkyl chains may enhance the stacking of the ATT cores due to additional van der Waals interactions stemming from the side chains. This allows aggregation of the ATT molecules into one-dimensional nanowire-like ensembles having highly anisotropic charge transport properties. Crystallization of those aggregates within the HTM films are expected to be oriented within the horizontal plane and thus compromising the vertical charge transport properties in the device. Increased crystallinity for ATT molecules with longer alkyl chains could also be the reason for less good film formation, which might also contribute to their lower conductivity and thus low device performance. Optical microscope images of the different HTM layers are shown in the SI.
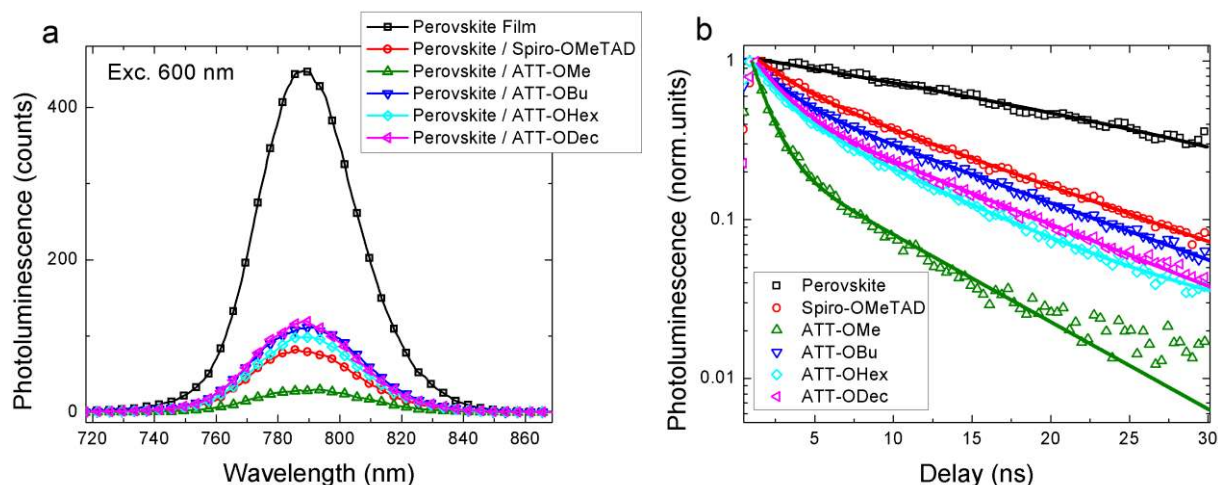
Figure 6. (a) CW photoluminescence spectra, excitation at 600 nm; and (b) time-resolved photoluminescence decay at 780 nm for the pristine perovskite film (black squares) deposited on glass, perovskite/spiro-OMeTAD sample (red dots) and perovskite/HTM as listed in the figure legend. Excitation at λ_{exc} = 460 nm, excitation density of 10 nJ cm^{-2}. All the samples have been encapsulated to prevent degradation or any oxygen/moisture induced effects. Solid lines represent the fitting curve resulting from exponential fitting in the form of y = A_1 exp(x/t_1)+A_2 exp(x/t_2).

The gain insight into the dynamics of hole transfer at the perovskite/HTM interface, we monitor the perovskite steady state and time-resolved photoluminescence (PL). **Figure 6a** shows the comparison of the PL spectra measured on pristine perovskite film and the one from perovskite interfaced with spiro-OMeTAD as well as with the series of the new molecules presented. The perovskite samples have a comparable thickness of 300 nm. This enables us to retain a constant density of absorbed photons for all the samples investigated. The continuous wave (CW) PL spectra of the perovskite/HTMs show a significant reduction of the PL signal with respect to the pristine perovskite film. The quenching is indicative of interfacial hole transfer that is similarly observed for all the HTMs, with a slightly enhanced quenching for the perovskite/ ATT-OMe molecule. To dynamically monitor this process, we investigated the time-resolved PL (**Figure 6b**). The pristine perovskite film shows a long-living decay fitted with a mono-exponential time constant above our time window of 30 ns, in agreement with what was previously observed in the literature.[37,38] On the other hand, the PL decays at the perovskite/spiro-OMeTAD and perovskite/ATT interfaces exhibit faster dynamics. Two time constants are retrieved from fitting, one comparable to the resolution of the instrument of around 1 ns, and a slower one of few nanoseconds (see Table 4). They show a similar trend to what observed for spiro-OMeTAD, with the slightly faster component for the ATT-OMe having a dominant amplitude ($A_1 = 87\%$). The quenching observed supports an efficient interfacial hole transfer. This behavior also suggests that the new molecules can effectively quench the PL, thus representing efficient hole-transfer materials, similar in function to spiro-OMeTAD. In addition, the interfacial dynamics further confirm the favorable hole transfer as one should expect from the relative energy position of the HOMO level of the synthesized HTMs. Other parameters, such as their mobility, their structure and their interfacial adhesion, must then also be considered to fully explain the different device efficiencies obtained.

Table 4. Time-resolved PL decay fitting parameters.

Sample	t_1 (ns)	t_2 (ns)	A_1 (%)	A_2 (%)
Perovskite	30		100	0
Spiro-OMeTAD	1.8	8.7	40	60
ATT-OMe	1	6	87	13
ATT-OBu	1.5	8.4	48	52
ATT-OHex	1.2	6	60	40
ATT-ODec	1.4	7.7	64	36

Conclusions

In summary, we present the synthesis and characterization of a series of new easily attainable hole-transporting materials based on an anthra[1,2-b:4,3-b′:5,6-b″:8,7-b‴]tetrathiophene for highly efficient PSCs. Devices prepared with ATT-OMe showed efficiencies of up to 18.1 %, closely matching the performance of *spiro*-OMeTAD, that is commonly used as a reference. Compared to *spiro*-OMeTAD, the ATT-based molecules are thermally more stable and are purified in a simple and non-expensive manner. They are good electron donors, similar to *spiro*-OMeTAD, and show a very small hole reorganization energy (0.096 eV). In addition, ATT-OMe exhibits slightly higher conductivity than *spiro*-OMeTAD. From the PL investigation we observe strong quenching of the perovskite PL signal employing the ATT molecules as well as for spiro-OMeTAD. A slightly faster quenching is observed in particular at the perovskite/ATT-OMe interface, while the rest of the ATT molecules behave indeed very similar to spiro-OMeTAD. All these features support the potential of ATT derivatives as HTMs. The effect of attaching alkyl chains of increasing length to the ATT molecules as "solubilizers" on the performance of the PSC devices has also been investigated. Although a great improvement of solubility is observed when attaching long alkyl chains on the triarylamines, the device performance is significantly decreased. We believe that the presence of alkyl chains enhances the stacking of the ATT cores in the HTM layer but decreasing, in turn, the hole-transport properties. Importantly, besides the low solubility of ATT-OMe, this can be heated and spin coated at 100 °C without affecting its performance. On the contrary,

when *spiro*-OMeTAD is heated to temperatures higher than 70 °C its efficiency dramatically

decreases. The findings of this work may benefit the future design of new HTM materials.

Supporting Information
Supporting Information is available from the Wiley Online Library or from the author.

[1]   A. Kojima, K. Teshima, Y. Shirai, T. Miyasaka, *J. Am. Chem. Soc.* **2009**, *131*, 6050.
[2]   M. Liu, M. B. Johnston, H. J. Snaith, *Nature* **2013**, *501*, 395.
[3]   J. Burschka, N. Pellet, S. J. Moon, R. Humphry-Baker, P. Gao, M. K. Nazeeruddin, M. Gratzel, *Nature* **2013**, *499*, 316.
[4]   D. B. Mitzi, in *Progress in Inorganic Chemistry*, John Wiley & Sons, Inc., 1999, 1.
[5]   L. Zheng, Y. Ma, S. Chu, S. Wang, B. Qu, L. Xiao, Z. Chen, Q. Gong, Z. Wu, X. Hou, *Nanoscale* **2014**, *6*, 8171.
[6]   V. D'Innocenzo, G. Grancini, M. J. P. Alcocer, A. R. S. Kandada, S. D. Stranks, M. M. Lee, G. Lanzani, H. J. Snaith, A. Petrozza, *Nat. Commun.* **2014**, *5,* 3586.
[7]   Y. Li, W. Yan, Y. Li, S. Wang, W. Wang, Z. Bian, L. Xiao, Q. Gong, *Sci. Rep.* **2015**, *5*, 14485.
[8]   Y.-C. Hsiao, T. Wu, M. Li, Q. Liu, W. Qin, B. Hu, *J. Mater. Chem. A* **2015**, *3*, 15372.
[9]   N. R. E. L. National Renewable Energy Laboratory, **2016**.
[10]   G. E. Eperon, S. D. Stranks, C. Menelaou, M. B. Johnston, L. M. Herz, H. J. Snaith, *Energy Environ. Sci.* **2014**, *7*, 982.
[11]   N. J. Jeon, J. H. Noh, W. S. Yang, Y. C. Kim, S. Ryu, J. Seo, S. I. Seok, *Nature* **2015**, *517*, 476.
[12]   M. Saliba, T. Matsui, J.-Y. Seo, K. Domanski, J.-P. Correa-Baena, M. K. Nazeeruddin, S. M. Zakeeruddin, W. Tress, A. Abate, A. Hagfeldt, M. Gratzel, *Energy Environ. Sci.* **2016**, *9*, 1989.
[13]   Y. Jo, K. S. Oh, M. Kim, K.-H. Kim, H. Lee, C.-W. Lee, D. S. Kim, *Adv. Mater. Interfaces* **2016**, *3*, DOI: 10.1002/admi.201500768.
[14]   J.-W. Lee, H.-S. Kim, N.-G. Park, *Acc. Chem. Res.* **2016**, *49,* 311.
[15]   P. Qin, S. Tanaka, S. Ito, N. Tetreault, K. Manabe, H. Nishino, M. K. Nazeeruddin, M. Grätzel, *Nat. Commun.* **2014**, *5,* 3834.

[16]   S. Ye, W. Sun, Y. Li, W. Yan, H. Peng, Z. Bian, Z. Liu, C. Huang, *Nano Lett.* **2015**, *15*, 3723.

[17]   G. A. Sepalage, S. Meyer, A. Pascoe, A. D. Scully, F. Huang, U. Bach, Y.-B. Cheng, L. Spiccia, *Adv. Funct. Mater.* **2015**, *25*, 5650.

[18]   T. Malinauskas, M. Saliba, T. Matsui, M. Daskeviciene, S. Urnikaite, P. Gratia, R. Send, H. Wonneberger, I. Bruder, M. Graetzel, V. Getautis, M. K. Nazeeruddin, *Energy Environ. Sci.* **2016**, *9*, 1681.

[19]   F. Zhang, C. Yi, P. Wei, X. Bi, J. Luo, G. Jacopin, S. Wang, X. Li, Y. Xiao, S. M. Zakeeruddin, M. Grätzel, *Adv. Energy Mater.* **2016**, DOI: 10.1002/aenm.201600401.

[20]   B. Xu, D. Bi, Y. Hua, P. Liu, M. Cheng, M. Gratzel, L. Kloo, A. Hagfeldt, L. Sun, *Energy Environ. Sci.* **2016**, *9*, 873.

[21]   K. Rakstys, M. Saliba, P. Gao, P. Gratia, E. Kamarauskas, S. Paek, V. Jankauskas, M. K. Nazeeruddin, *Angew. Chem. Int. Ed.* **2016**, *55*, 7464.

[22]   L. Cabau, I. Garcia-Benito, A. Molina-Ontoria, N. F. Montcada, N. Martin, A. Vidal-Ferran, E. Palomares, *Chem. Commun.* **2015**, *51*, 13980.

[23]   Y.-K. Wang, Z.-C. Yuan, G.-Z. Shi, Y.-X. Li, Q. Li, F. Hui, B.-Q. Sun, Z.-Q. Jiang, L.-S. Liao, *Adv. Funct. Mater.* **2016**, *26*, 1375.

[24]   S. Park, J. H. Heo, J. H. Yun, T. S. Jung, K. Kwak, M. J. Ko, C. H. Cheon, J. Y. Kim, S. H. Im, H. J. Son, *Chem. Sci.* **2016**, DOI:10.1039/C6SC00876C.

[25]   P. Gratia, A. Magomedov, T. Malinauskas, M. Daskeviciene, A. Abate, S. Ahmad, M. Grätzel, V. Getautis, M. K. Nazeeruddin, *Angew. Chem. Int. Ed.* **2015**, *54*, 11409.

[26]   H. Li, K. Fu, A. Hagfeldt, M. Grätzel, S. G. Mhaisalkar, A. C. Grimsdale, *Angew. Chem. Int. Ed.* **2014**, *53*, 4085.

[27]   S. Kazim, F. J. Ramos, P. Gao, M. K. Nazeeruddin, M. Grätzel, S. Ahmad, *Energy Environ. Sci.* **2015**, *8*, 1816.

[28]   K. Rakstys, A. Abate, M. I. Dar, P. Gao, V. Jankauskas, G. Jacopin, E. Kamarauskas, S. Kazim, S. Ahmad, M. Grätzel, M. K. Nazeeruddin, *J. Am. Chem. Soc.* **2015**, *137*, 16172.

[29]   J. Cao, Y. M. Liu, X. Jing, J. Yin, J. Li, B. Xu, Y. Z. Tan, N. Zheng, *J. Am. Chem. Soc.* **2015**, *137*, 10914.

[30]   A. Molina-Ontoria, I. Zimmermann, I. Garcia-Benito, P. Gratia, C. Roldán-Carmona, S. Aghazada, M. Graetzel, M. K. Nazeeruddin, N. Martín, *Angew. Chem. Int. Ed.* **2016**, *55*, 6270.

[31]   M. Saliba, S. Orlandi, T. Matsui, S. Aghazada, M. Cavazzini, J.-P. Correa-Baena, P. Gao, R. Scopelliti, E. Mosconi, K.-H. Dahmen, F. De Angelis, A. Abate, A. Hagfeldt, G. Pozzi, M. Graetzel, M. K. Nazeeruddin, *Nat. Energy* **2016**, *1*, 15017.

[32]   J. L. Brusso, O. D. Hirst, A. Dadvand, S. Ganesan, F. Cicoira, C. M. Robertson, R. T. Oakley, F. Rosei, D. F. Perepichka, *Chem. Mater.* **2008**, *20*, 2484.

[33]   W.-J. Liu, Y. Zhou, Y. Ma, Y. Cao, J. Wang, J. Pei, *Org. Lett.* **2007**, *9*, 4187.

[34]   Y. Yao, H. Dong, W. Hu, *Adv. Mater.* **2016**, *28*, 4513.

[35]   A. N. Sokolov, S. Atahan-Evrenk, R. Mondal, H. B. Akkerman, R. S. Sánchez-Carrera, S. Granados-Focil, J. Schrier, S. C. B. Mannsfeld, A. P. Zoombelt, Z. Bao, A. Aspuru-Guzik, *Nat. Commun.* **2011**, *2*, 437.

[36]   D. Bi, W. Tress, M. I. Dar, P. Gao, J. Luo, C. Renevier, K. Schenk, A. Abate, F. Giordano, J.-P. Correa Baena, J.-D. Decoppet, S. M. Zakeeruddin, M. K. Nazeeruddin, M. Grätzel, A. Hagfeldt, *Sci. Adv.* **2016**, *2*, e1501170.

[37]   C. Roldán-Carmona, P. Gratia, I. Zimmermann, G. Grancini, P. Gao, M. Graetzel and M. K. Nazeeruddin, *Energy Environ. Sci.*, **2015**, *8*, 3550.

[38]   E. Mosconi, G. Grancini, C. Roldán-Carmona, P. Gratia, I. Zimmermann, M. K. Nazeeruddin, and F. De Angelis, *Chem. Mater.*, Just Accepted Manuscript DOI: 10.1021/acs.chemmater.6b00779.

A sulfur-rich polycyclic aromatic hydrocarbon with a flat and rigid π conjugated structure endowed with triarylamine groups is synthesized for highly efficient perovskites solar cells. The influence of alkyl chains often introduced to increase the solubility of the HTMs is furthermore investigated. Remarkable efficiencies are obtained.

hole-transporting materials, perovskite solar cells, anthratetrathiophenes, alkyl chains

Iwan Zimmermann,† Javier Urieta-Mora,† Paul Gratia, Juan Aragó, Giulia Grancini, Agustín Molina-Ontoria,* Enrique Ortí,* Nazario Martín,* Mohammad Khaja Nazeeruddin*

High-Efficiency Perovskite Solar Cells using Molecularly-Engineered, Thiophene-Rich, Hole-Transporting Materials: Influence of Alkyl Chain Length on Power Conversion Efficiency

HTMs	FF %)	PCE (%)
ATT-OMe	78.1	18.13
ATT-OBu	78.3	17.28
ATT-OHex	77.8	15.66
ATT-ODec	62.9	9.67

WILEY-VCH
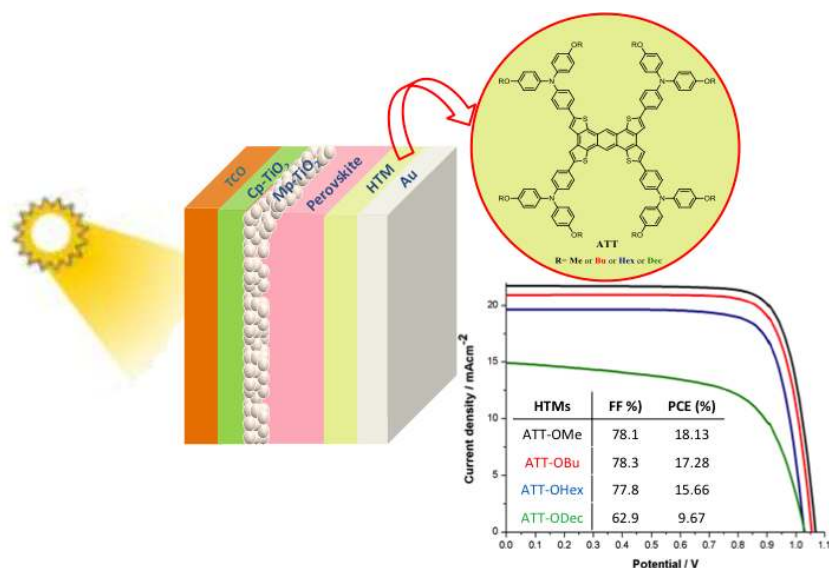
Supporting Information

High-Efficiency Perovskite Solar Cells using Molecularly-Engineered, Thiophene-Rich, Hole-Transporting Materials: Influence of Alkyl Chain Length on Power Conversion Efficiency

Iwan Zimmermann,[†] Javier Urieta-Mora,[†] Paul Gratia, Juan Aragó, Giulia Grancini, Agustín Molina-Ontoria, Enrique Ortí,* Nazario Martín,* Mohammad Khaja Nazeeruddin**

This work is dedicated to the memory of Harold W. Kroto

Dr. I. Zimmermann, P. Gratia, Dr. G. Grancini and Prof. M. K. Nazeeruddin
Group for Molecular Engineering of Functional Materials
and Laboratory for Photonics and Interfaces
EPFL VALAIS, CH-1951 Sion, Switzerland
E-mail: mdkhaja.nazeeruddin@epfl.ch

J. Urieta-Mora, Dr. A. Molina-Ontoria, Prof. N. Martín
IMDEA-Nanociencia
C/ Faraday 9, Ciudad Universitaria de Cantoblanco
28049 Madrid, Spain
E-mail: nazmar@ucm.es

J. Urieta-Mora, Prof. N. Martín.
Departamento Química Orgánica, Facultad C. C. Químicas
Universidad Complutense de Madrid
Av. Complutense s/n, 28040 Madrid (Spain)
Homepage: http://www.ucm.es/info/fullerene/

Dr. J. Aragó, Prof. E. Ortí
Instituto de Ciencia Molecular
Universidad de Valencia
Catedrático José Beltrán 2, 46980, Paterna (Spain)

1. **Experimental**

2. **Synthetic details and characterization**

3. **Computational Details**

4. **Device preparation**

5. **Solar cell characterization**

   5.1 EQE

   5.2 Hysteresis plots

   5.3 Device statistics

   5.4 Photoluminescence

6. **Supplementary figures**

   6.1 DSC

   6.2 NMR, MS

   6.3 HTM layers

1. Experimental Section

General Methods. Chemicals and reagents were purchased from commercial suppliers and used as received. All solvents were dried according to standard procedures. Air-sensitive reactions were carried out under argon atmosphere. The device preparation was done in a glovebox under nitrogen atmosphere. Flash chromatography was performed using silica gel (Merck, Kieselgel 60, 230-240 mesh or Scharlau 60, 230-240 mesh). Analytical thin layer chromatography (TLC) was performed using aluminum-coated Merck Kieselgel 60 F254 plates. NMR spectra were recorded on a Bruker Advance 300 (^{1}H: 400 MHz; ^{13}C: 101 MHz) spectrometer at 298 K using partially deuterated solvents as internal standards. Coupling constants (J) are denoted in Hz and chemical shifts (δ) in ppm. Multiplicities are denoted as follows: s = singlet, d = doublet, t = triplet, m = multiplet. FT-IR spectra were recorded on a Bruker Tensor 27 (ATR device) spectrometer. UVVis spectra were recorded in a Varian Cary 50 spectrophotometer. Mass spectra Matrix assisted Laser desorption ionization (coupled to a Time-of-Flight analyzer) experiments (MALDI-TOF) were recorded on a MAT 95 thermo spectrometer and a Bruker REFLEX spectrometer respectively. Cyclic voltammetry (CV) experiments were conducted in 0.1 M solution of NBu_4PF_6 in DCM. Glassy carbon electrode was used as a working electrode and platinum wires were used as counter and reference electrodes. Before each measurement, solutions were deoxygenated with N_2. Ferrocene was added as an internal standard; its oxidation potential in DCM was positioned at 0.7 V *vs.* NHE and HTMs' oxidation potential were recalculated in reference to NHE. Thermogravimetric analysis (TGA) was performed using a TA Instruments TGAQ500 with a ramp of 10 °C/min under N_2 from 100 to 1000 °C. DSC was run on a Discovery DSC from TA instruments. Three cycles were recorded under nitrogen, heating (until 400 °C) and cooling (50 °C) at 20 °C/min of scanning rate.

2. Synthetic details and characterization

Compounds **2**, **3** and **4** were prepared according to previously reported synthetic procedures [see: a) *Chem. Mater.* **2008***, 20, 2482-2494*, and showed identical spectroscopic properties to those reported therein. 4-(4,4,5,5-Tetramethyl-1,3,2-dioxaborolan-2-yl)-N,N-bis(4-decyloxyphenyl)aniline was synthesized following the same protocol as 4-(4,4,5,5-Tetramethyl-1,3,2-dioxaborolan-2-yl)-N,N-bis(4-methoxyphenyl)aniline which is illustrated below (scheme S-2, showing the expected resonance signals of the aliphatic and aromatic protons and carbons.
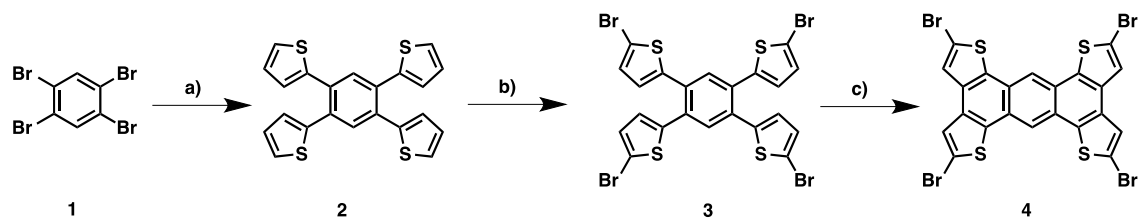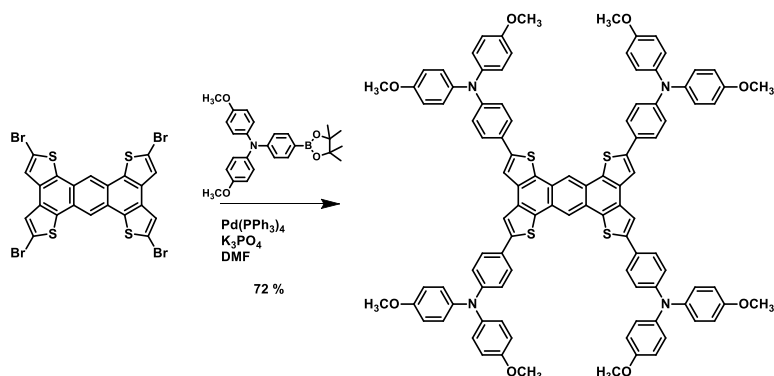
Scheme S1. *Reagents and conditions: a) 2-(tributylstannyl)thiophene, Pd(PPh₃)₂Cl₂, DMF, 130 ℃, 92 %; b) NBS, THF, rt, 82 %; c)FeCl₃, MeNO₂/ClPh, rt, 99 %.*
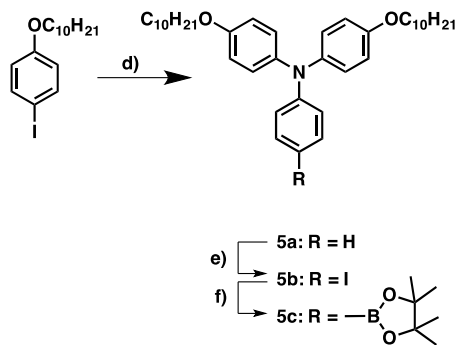
Scheme S2. *Reagents and conditions: d) Aniline, Pd₂(dba)₃, XPhos, Toluene, ᵗBuONa, 105 ℃, 83 % ; e) I₂, H₅IO₆, EtOH, rt, 81 %; f) Pd(dppf)Cl₂·CH₂Cl₂ , Bpin, KOAc, DMF, 80 ℃, 78 %.*
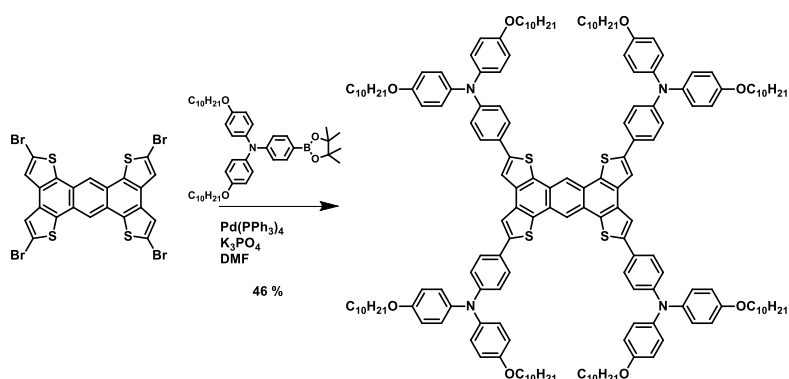
ATT-OMe

A solution of **4** (250 mg, 0.35 mmol), 4-(4,4,5,5-tetramethyl-1,3,2-dioxaborolan-2-yl)-N,N-bis(4-methoxyphenyl)aniline (675.7 mg, 1.56 mmol), K_3PO_4 (1.78 g, 8.4 mmol) and $Pd(PPh_3)_4$ (80.9 mg, 0.07 mmol) in DMF (8 mL) was degassed for 1 hour under nitrogen. The reaction was heated at 100 °C for 4 hours. The mixture was cooled to room temperature and water was added. The resulting precipitate was filtered and washed with water and dissolved in hot chloroform. The organic phase was dried over sodium sulfate. The solvent was removed under reduced pressure and the crude product was purified by flash column chromatography (silica gel, CH_2Cl_2 and then CH_2Cl_2:AcOEt (120:1)) to afford **ATT-OMe** as a orange solid (395 mg, 0.25 mmol), yield 72 %. ^{1}H NMR (400 MHz, THF) δ/ppm 8.67 (s, 2H), 7.99 (s, 4H), 7.70 (d, J = 8.7 Hz, 8H), 7.15-7.11 (m, 16H), 7.01 (d, J = 8.7Hz, 8H), 6.94-6.90 (m, 16H), 3.82 (s, 24H); ^{13}C NMR (176 MHz, THF-d8) δ/ppm 156.5, 148.9, 144.3, 140.4, 134.6, 133.1, 126.7, 126.5, 125.1, 119.9, 117.38, 114.6, 54.6; FTIR (neat): 2996, 2927, 1603, 1501, 1320, 1276, 1034, 820 cm^{-1}; HRMS calcd for $C_{102}H_{78}N_4O_8S_4[M^+]$, 1614.4697; found 1614.4748.

ATT-OBu
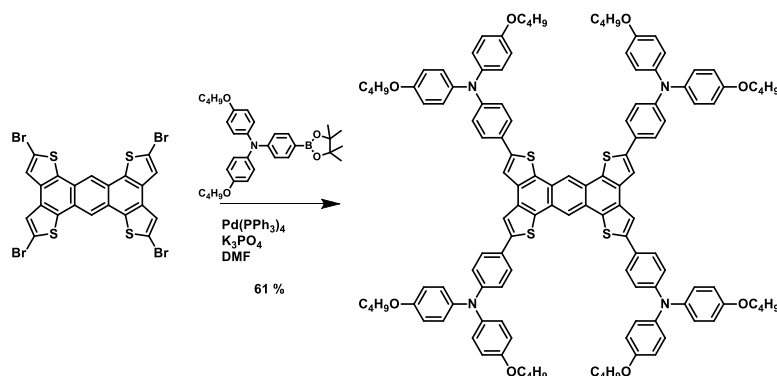
A solution of **4** (178 mg, 0.25 mmol), 4-(4,4,5,5-tetramethyl-1,3,2-dioxaborolan-2-yl)-N,N-bis(4-butyloxyphenyl)aniline (550 mg, 1.06 mmol), K_3PO_4 (1.26 g, 5.95 mmol) and Pd(PPh$_3$)$_4$ (57 mg, 0.05 mmol) in DMF (6 mL) was degassed for 1 hour under nitrogen. The reaction was heated at 110 °C for 3 hours. The mixture was cooled to room temperature and water was added. The resulting precipitate was filtered and washed with water and dissolved in hot chloroform. The organic phase was dried over sodium sulfate. The solvent was removed under reduced pressure and the crude product was purified by flash column chromatography (silica gel, CH$_2$Cl$_2$ to afford **ATT-OBu** as a yellow solid (245 mg, 0.25 mmol), yield 61 %. ^{1}H NMR (400 MHz, THF) δ/ppm 8.49 (s, 2H), 7.85 (s, 4H), 7.62 (d, J = 8.7 Hz, 8H), 7.08-7.04 (m, 16H), 6.96 (d, J = 8.7 Hz, 8H), 6.88-6.84 (m, 16H), 3.96 (t, J = 6.6 Hz, 16H), 1.80-1.73 (m, 16H), 1.57-1.48 (m, 16H), 1.01 (t, J = 6.6 Hz, 24H); ^{13}C NMR (101 MHz, CDCl$_3$) δ/ppm 155.6, 148.4, 143.8, 140.4, 133.8, 133.5, 126.8, 126.7, 126.3, 124.8, 120.2, 117.7, 117.0, 115.3, 67.9, 31.4, 19.3, 13.9; FTIR (neat): 2957, 2934, 1602, 1504, 1488, 1263, 973, 825 cm^{-1}; HRMS calcd for C$_{126}$H$_{126}$N$_4$O$_8$S$_4$, [M$^+$], 1950.8453; found 1950.8402.

ATT-OHex
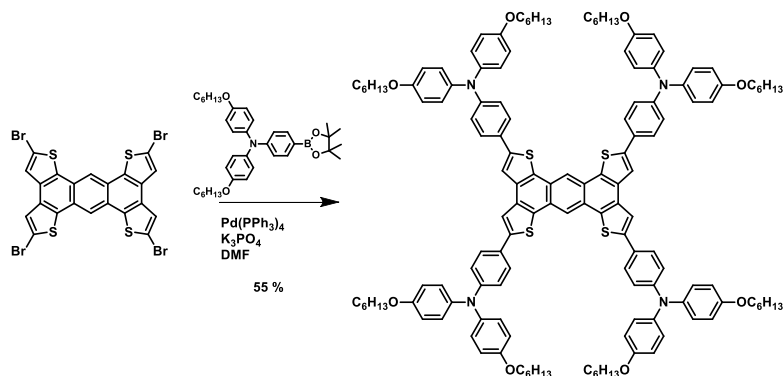
A solution of **4** (207 mg, 0.29 mmol), 4-(4,4,5,5-tetramethyl-1,3,2-dioxaborolan-2-yl)-N,N-bis(4-hexyloxyphenyl)aniline (740 mg, 1.29mmol), K_3PO_4 (1.46 g, 6.91 mmol) and Pd(PPh$_3$)$_4$ (66.6 mg, 0.06 mmol) in DMF (6 mL) was degassed for 1 hour under nitrogen. The reaction was heated at 130 °C for 3 hours. The mixture was cooled to room temperature and water was added. The resulting precipitate was filtered and washed with water and dissolved in hot chloroform. The organic phase was dried over sodium sulfate. The solvent was removed under reduced pressure and the crude product was purified by flash column chromatography (silica gel, CH_2Cl_2:Hexane (4:1) to afford **ATT-OHex** as a yellow solid (395 mg, 0.25 mmol), yield 55 %. ^{1}H NMR (400 MHz, THF-d8) δ/ppm 8.64 (s, 2H), 7.96 (s, 4H), 7.66 (d, J = 8.7 Hz, 8H), 7.09-7.05 (m, 16H), 6.97 (d, J = 8.7Hz, 8H), 6.89-6.85 (m, 16H), 3.95 (t, J = 6.6 Hz, 16H), 1.81-1.75 (m, 16H), 1.54-1.36 (m, 48H), 0.95-0.93 (m, 24H); ^{13}C NMR (101 MHz, CDCl$_3$) δ/ppm 155.6, 148.5, 143.9, 140.4, 134.0, 133.5, 126.9, 126.8, 126.3, 124.9, 120.2, 117.8, 117.1, 115.3, 68.3, 31.7, 29.4, 25.8, 22.7, 14.1; FTIR (neat): 3037, 2927, 1604, 1500, 1320, 1270, 1235, 1024, 818 cm^{-1}; HRMS calcd for $C_{142}H_{158}N_4O_8S_4$[M$^+$], 2175.0957; found 2175.1001.

ATT-ODec

A solution of **4** (175 mg, 0.24 mmol), 4-(4,4,5,5-tetramethyl-1,3,2-dioxaborolan-2-yl)-N,N-bis(4-decyloxyphenyl)aniline (750 mg, 1.09 mmol), K_3PO_4 (1.24 g, 5.84 mmol) and $Pd(PPh_3)_4$ (56.6 mg, 0.05 mmol) in DMF (6 mL) was degassed for 1 hour under nitrogen. The reaction was heated at 130 °C for 3 hours. The mixture was cooled to room temperature and water was added. The resulting precipitate was filtered and washed with water and dissolved in hot chloroform. The organic phase was dried over sodium sulfate. The solvent was removed under reduced pressure and the crude product was purified by flash column chromatography (silica gel, CH_2Cl_2:hexane (3:7) and then CH_2Cl_2:hexane (7:3) to afford **ATT-ODec** as a yellow solid (292 mg, 0.25 mmol), yield 46 %. ^{1}H NMR (400 MHz, THF-d8) δ/ppm 8.79 (s, 2H), 8.07 (s, 4H), 7.70 (d, J = 8.7Hz, 8H), 7.10-7.06 (m, 16H), 6.98 (d, J = 8.7Hz, 8H), 6.89-6.85 (m, 16H), 3.96 (t, J = 6.6 Hz, 16H), 1.81-1.29 (m, 64H), 0.90 (t, J = 6.6 Hz, 24H); ^{13}C NMR (101 MHz, $CDCl_3$) ^{13}C NMR (101 MHz, $CDCl_3$) δ/ppm 155.6, 148.5, 143.9, 140.3, 133.9, 133.5, 126.9, 126.8, 126.3, 126.1, 124.9, 120.2, 117.8, 117.1, 115.3, 68.2, 31.9, 29.7, 29.6, 29.5, 29.4, 29.3, 26.1, 22.7, 14.1; FTIR (neat): 2922, 2853, 1601, 1504, 1487, 1238, 852 cm^{-1}; HRMS calcd for. $C_{174}H_{222}N_4O_8S_4[M^+]$, 2623.5965; found 2623.6028.

3. Computational details

All quantum-chemical calculations were carried out with the Gaussian 09 (revision D.01) software package.[1] Geometry optimization of the ATT core, the OMeTPA addends and the ATT-OMe and *spiro*-OMeTAD compounds were performed within the density functional theory (DFT) framework using the B3LYP functional[2] and the 6-31G** basis set.[3] D_{2h}, C_2, C_2 and C_2 symmetry constrains were imposed during the optimizations for ATT, OMeTPA, ATT-OMe and *spiro*-OMeTAD, respectively. Vertical electronic transition energies to the lowest-energy singlet excited states were computed for ATT, OMeTPA and ATT-OMe using the time-dependent DFT (TD-DFT) approach and the ground-state optimized geometries.[4] The lowest 20 singlet excited states were calculated at the B3LYP/6-31G** level. Geometry optimizations of the radical cations of ATT, OMeTPA, ATT-OMe and *spiro*-OMeTAD were performed to evaluate the hole reorganization energy (the procedure used is explained below). Radical cations are treated as open-shell systems and computed within the spin-unrestricted DFT approximation at the UB3LYP/6-31G** level. Molecular orbitals were plotted using the Chemcraft 1.6 software with isovalue contours of ±0.03 a.u.[5]

Figure S3.1 presents a schematic drawing of the potential energy surfaces for the neutral and cation states of two molecules (labelled as 1 and 2) involved in a charge transfer process. The intramolecular reorganization energy (λ) consists of two terms related to the geometry relaxation energies of one molecule going from the fully relaxed ground state of the neutral species to the cation state (Figure S3.1, left) and a neighbouring molecule evolving in the opposite way (Figure S3.1, right),

$$\lambda = \lambda_1 + \lambda_2 \tag{1}$$

$$\lambda_1 = E\ (M1) - E\ (M1^+) \tag{2}$$

$$\lambda_2 = E\ (M2^+) - E\ (M2) \tag{3}$$

Here, $E\ (M1)$ and $E\ (M1^+)$ for molecule 1 are the energies of the positively charged molecule (the cation) at the equilibrium geometry of the neutral molecule and the relaxed cation, respectively, and $E\ (M2^+)$ and $E\ (M2)$ for molecule 2 are, accordingly, the energies of the neutral molecule at the equilibrium geometry of the cation and the neutral molecule, respectively.
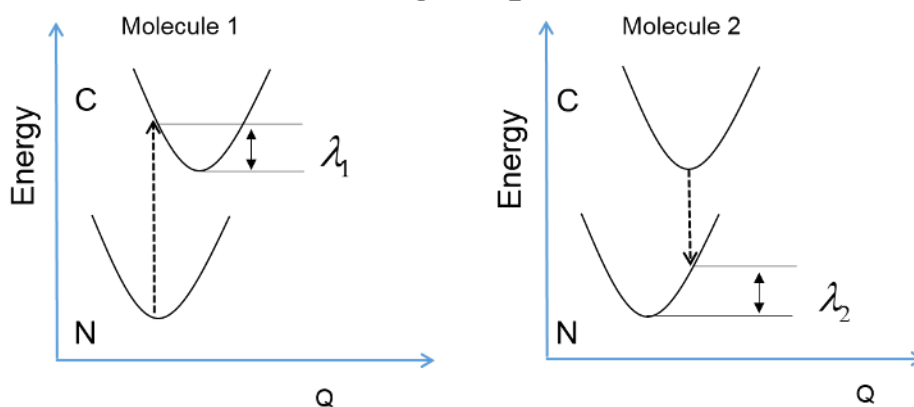
$$\lambda = \lambda_1 + \lambda_2$$

Figure S3.1. Scheme of the potential energy surfaces of the neutral state (N) and the cation state (C) for two molecules (1 and 2) involved in a charge (hole) transfer process. λ_1 and λ_2 are the two contributions to the total intramolecular reorganization energy (λ).

It is worth explaining why the reorganization energy for the ATT-OMe compound is smaller (0.096 eV) than that calculated for the ATT core (0.126 eV). This apparently discrepancy can be easily enlightened by the analysis of the electronic structure, in particular the HOMO orbital, in both compounds (Figure S3.3). The HOMO of ATT-OMe is not only localized on the conjugated core but also spreads over the OMeTPA groups (the phenyl rings attached to the ATT core and the nitrogen atoms). Therefore, the removal of an electron (mainly from the HOMO) in ATT-OMe in comparison with the ATT core involves a less structural reorganization change than that necessary for the ATT core. For instance, the length of the bonds fusing the thiophene rings to the anthracene unit change from 1.395 to 1.418 Å when forming the cation of the ATT core, whereas they only change from 1.396 to 1.402 Å for ATT-OMe. Note that in both compounds the core is completely planar. This finding is in agreement with the trends found in the family of the popular oligoacenes where the more electronic delocalization with the oligomer chain the less reorganization energy obtained.[6]

Figure S3.2 displays the B3LYP/6-31G**-optimized structure of the ATT-OMe compound. ATT-OMe exhibits an extended π-conjugated structure; the ATT core is planar and the dihedral angle between the phenyl rings connecting the peripheral OMeTPA groups and the thiophene rings of the ATT core are of 23.5°. Despite the bulky terminal OMeTPA groups, ATT-OMe exhibits a quite planar stucture that, in principle, can give rise to stacking aggregation in the solid state. Table S1 collects the vertical excitation energies (*E*), oscillator strengths (*f*) and electronic descriptions in terms of one-electron molecular orbital excitations calculated for the most intense singlet→singlet ($S_0 \rightarrow S_n$) transitions of ATT, OMeTPA and ATT-OMe. Figure S3.3 shows the molecular orbitals involved in the $S_0 \rightarrow S_n$ transitions quoted in Table S1.
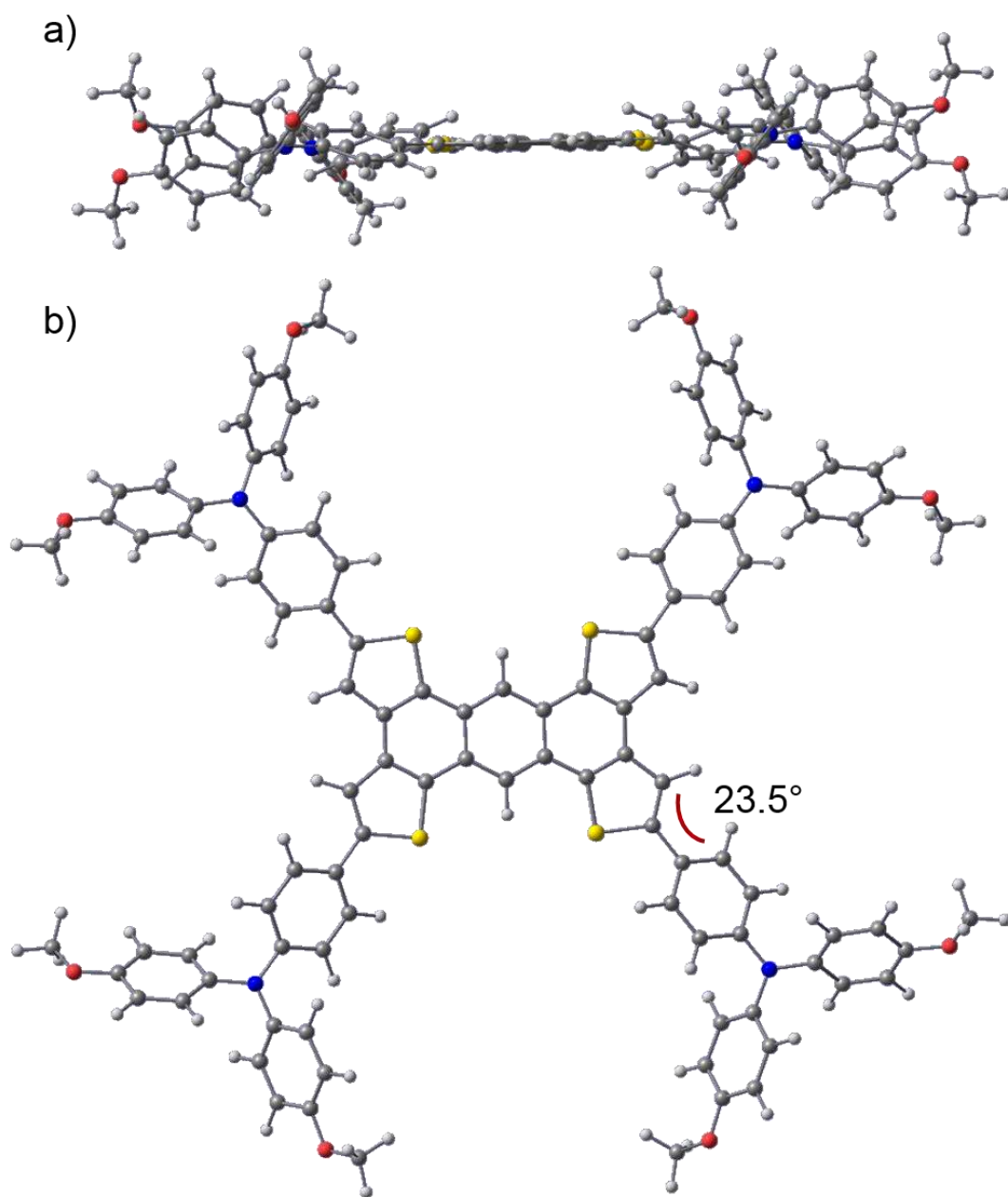
30

a)

b)

23.5°

Figure S3.2. Lateral (a) and top view (b) of the optimized geometry of the ATT-OMe compound at the B3LYP/6-31G** level.

Table S1. Vertical excitation energies (E), oscillator strengths (f) and electronic descriptions calculated for ATT, OMeTPA and ATT-OMe compounds at TD-DFT B3LYP/6-31G** level.

Compound	State	E (nm)	E (eV)	f	Description[a]
ATT	S_1	404	3.07	0.004	H → L
	S_2	393	3.15	0.058	H-1 → L
	S_4	321	3.87	1.258	H → L+1
	S_5	307	4.04	0.146	H-1 → L+1
OMeTPA	S_1	340	3.64	0.026	H → L
	S_2	309	4.02	0.225	H → L+1
	S_4	299	4.14	0.310	H → L+2
	S_5	297	4.17	0.075	H → L+3
ATT-OMe	S_1	498	2.49	0.528	H-1 → L
	S_2	495	2.50	0.353	H → L
	S_3	458	2.71	1.600	H → L+1
	S_6	440	2.82	1.150	H-1 → L+1
	S_9	400	3.13	0.164	H-5 → L
	S_{10}	383	3.24	0.237	H-4 → L
	S_{14}	360	3.45	0.563	H-4 → L+1
	S_{15}	358	3.47	0.6402	H-2 → L+2

[a] H and L denotes HOMO and LUMO, respectively.

It should be mentioned that the lowest-energy $S_0 \rightarrow S_1$ electronic transition for AAT-OMe is mainly described by the HOMO-1 → LUMO monoexcitation (93 %), whereas the $S_0 \rightarrow S_2$ electronic transition is mainly associated with the HOMO → LUMO monoexcitation (96 %). This behavior where the lowest-energy transition is not described by the HOMO → LUMO excitation arises as a consequence of the quasi-degeneracy of the HOMO–1 (–4.48 eV) and HOMO (–4.45 eV) (Figure S3.3) and the participation of other monoexcitations with non-negligible contributions in both electronic transitions. Note that the $S_0 \rightarrow S_1$ (2.49 eV, 498 nm) and $S_0 \rightarrow S_2$ (2.50 eV, 495 nm) transitions, similarly to the HOMO–1 and HOMO, are also almost degenerate. These transitions, together with the $S_0 \rightarrow S_3$ and $S_0 \rightarrow S_6$, are jointly involved under the experimental absorption band peaking at 402 nm.
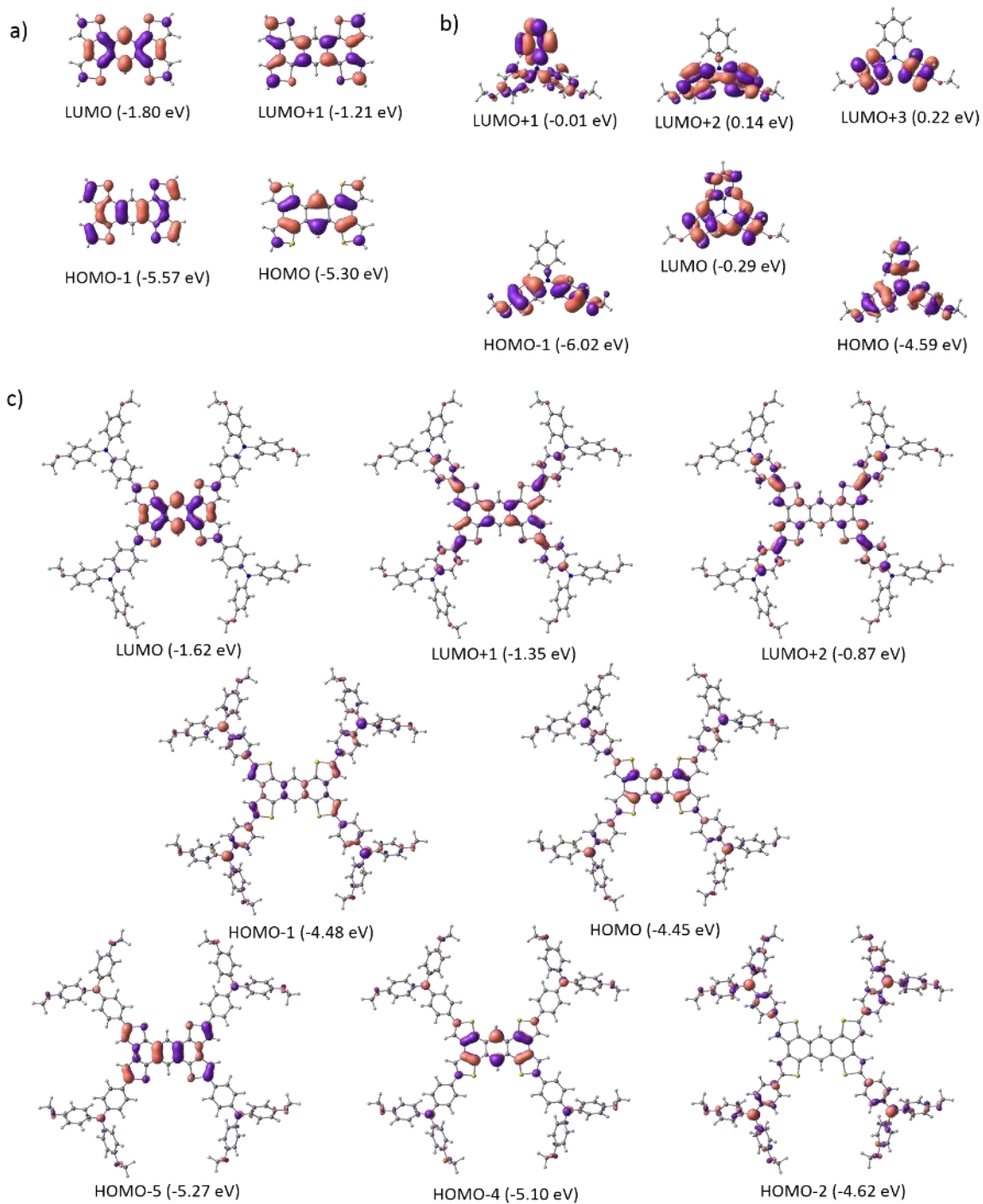
Figure S3.3. B3LYP/6-31G** isovalue contours (±0.03 a.u.) and energies calculated for selected MOs involved in the electronic transitions of ATT, OMeTPA and ATT-OMe.

1. Gaussian 09, Revision D.01, M. J. Frisch, G. W. Trucks, H. B. Schlegel, G. E. Scuseria, M. A. Robb, J. R. Cheeseman, G. Scalmani, V. Barone, B. Mennucci, G. A. Petersson, H. Nakatsuji, M. Caricato, X. Li, H. P. Hratchian, A. F. Izmaylov, J. Bloino, G. Zheng, J. L. Sonnenberg, M. Hada, M. Ehara, K. Toyota, R. Fukuda, J. Hasegawa, M. Ishida, T. Nakajima, Y. Honda, O. Kitao, H. Nakai, T. Vreven, J. A. Montgomery, J. E. Peralta, F. Ogliaro, M. Bearpark, J. J. Heyd, E. Brothers, K. N. Kudin, V. N. Staroverov, R. Kobayashi, J. Normand, K. Raghavachari, A. Rendell, J. C. Burant, S. S. Iyengar, J. Tomasi, M. Cossi, N. Rega, J. M. Millam, M. Klene, J. E. Knox, J. B. Cross, V. Bakken, C. Adamo, J. Jaramillo, R. Gomperts, R. E. Stratmann, O. Yazyev, A. J. Austin, R. Cammi, C. Pomelli, J. W. Ochterski, R. L. Martin, K. Morokuma, V. G. Zakrzewski, G. A. Voth, P. Salvador, J. J. Dannenberg, S. Dapprich, A. D. Daniels, Farkas, J. B. Foresman, J. V. Ortiz, J. Cioslowski, D. J. Fox, Gaussian, Inc., Wallingford CT, 2009.

2. a) C. Lee, W. Yang, R. G. Parr, *Phys. Rev. B* **1988**, *37*, 785-789; b) A. D. Becke, *J. Chem. Phys.* **1993**, *98*, 5648-5652.

3. M. M. Francl, W. J. Pietro, W. J. Hehre, J. S. Binkley, M. S. Gordon, D. J. Defrees, J. A. Pople, *J. Chem. Phys.* **1982**, *77*, 3654-3665.

4. a) M. E. Casida, C. Jamorski, K. C. Casida, D. R. Salahub, *J. Chem. Phys.* **1998**, *108*, 4439-4449; b) C. Jamorski, M. E. Casida, D. R. Salahub, *J. Chem. Phys.* **1996**, *104*, 5134-5147; c) M. Petersilka, U. J. Gossmann, E. K. U. Gross, *Phys. Rev. Lett.* **1996**, *76*, 1212-1215.

5. http://www.chemcraftprog.com

6. a) V. Coropceanu, M. Malagoli, D. A. da Silva Filho, N. E. Gruhn, T. G. Bill, J. L. Brédas, *Phys. Rev. Lett.* **2002**, *89*, 275503; b) W.-Q. Deng, W. A. Goddard, *J. Phys. Chem. B* **2004**, *108*, 8614-8621.

4. Device Preparation

Conductive FTO glass (NSG10) was sequentially cleaned by sonication in a 2 % Helmanex solution and isopropanol for 15 min respectively. A 30 nm titania blocking layer was applied on the substrates by spraying a solution of titanium diisopropoxide bis(acetylacetonate) in ethanol at 450 °C. For the 200–300 nm mesoporous TiO_2 layer, 30 NR-D titania paste from Dyesol diluted in ethanol (ratio 1:8 by weight) was applied by spin-coating at 2000 rpm for 10s followed by a sintering step at 500 °C for 20 min. After cooling down the substrates a Li-treatment was applied by spin-coating 60 µL of a solution of tris(bis(trifluoromethylsulfonyl)imide) (Li-TFSI) in acetonitrile (10 mg/mL) onto the mesoporous layer, followed by a sintering step at 500 °C for 10 min to decompose the Li-salt as previously described.[1] The perovskite layers were fabricated by a single step spin-coating procedure reported by Soek et al.[2] For the perovskite precursor solution 508 mg of PbI_2(TCI), 68 mg PbI_2 (TCI), 180.5 mg formamidinium iodide (Dyesol) and 20.7 mg methylammonium bromide (Dyesol) were dissolved in a 1:4 mixture of DMSO:DMF. The perovskite solution was spun at 5000 rpm for 30 s using a ramp of 3000 rpm/s. 15 s prior to the end of the spin-coating sequence 100 µL chlorobenzene were poured onto the spinning substrate. Afterwards the substrates were transferred onto a heating plate and annealed at 100 °C for 45 min. The hole-transporting materials were applied from solutions in chlorobenzene. Optimized concentrations were found to be 20 mM for ATT-OMe and 30 mM for ATT-OBu, ATT-OHex and ATT-ODec respectively. Tert-butylpyridine (Tbp), tris(2-(1H-pyrazol-1-yl)-4-tert-butylpyridine)cobalt(III) (FK209) and Li-TFSI were added as additives. Equimolar amounts of additives were added for all hole-transporters: 330 mol% Tbp, 50 mol% Li-TFSI from a 1.8 M stock solution in acetonitrile and 3 mol% FK209 from a 0.25 M stock solution in acetonitrile. The final HTM solutions were spin-coated dynamically onto the perovskite layers at 4000 rpm for 20 s. Due to the low solubility of ATT-OMe the HTM solution as well as the substrate were heated to 100 °C for spin coating. The gold electrodes were deposited by thermal evaporation of 100 nm gold using a shadow mask under high vacuum conditions.

[1]F. Giordano A. Abate, J.P. Correa-Baena, M. Saliba, T. Matsui, S. H. Im, S. M. Zakeeruddin, M. K. Nazeeruddin, A. Hagfeldt, M. Graetzel, Nat. Commun. 2016, 7, 10379.

[2]Jeon, N. J.; Noh, J. H.; Kim, Y. C.; Yang, W. S.; Ryu, S.; Seok, S. I. Nat. Mater. 2014, 13, 897.

5. Solar cell characterization

The photovoltaic device performance was analyzed using a VeraSol LED solar simulator (Newport) producing 1 sun AM 1.5 (100W/cm²) sunlight. Current-voltage curves were measured in air with a potentiostat (Keithley). The light intensity was calibrated with an NREL certified KG5 filtered Si reference diode. The solar cells were masked with a metal aperture of 0.16 cm² to define the active area. The current-voltage curves were recorded scanning at 20 mV s^{-1}.

5.1. EQE measurements

External quantum efficiency (EQE) measurements were performed with an IQE-200B Quantum Efficiency Measurement system from Newport in the range of 350 to 820 nm using a step size of 10 nm.
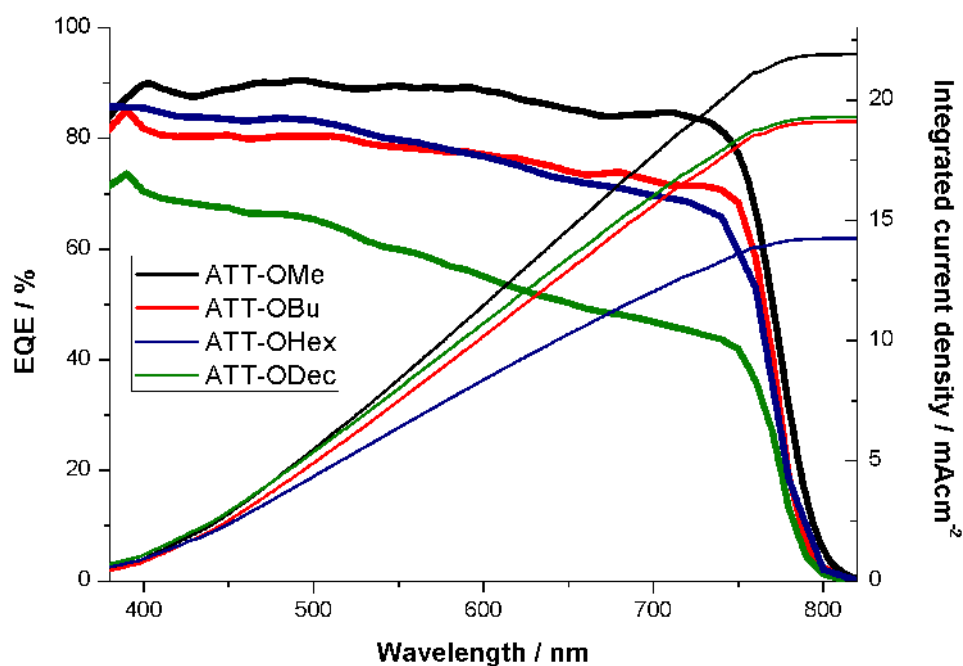
Figure 5.1.1. External quantum efficiency (EQE) and integrated current plots of ATT-OMe, ATT-OBu, ATT-OHex and ATT-ODec.

5.2 Hysteresis plots
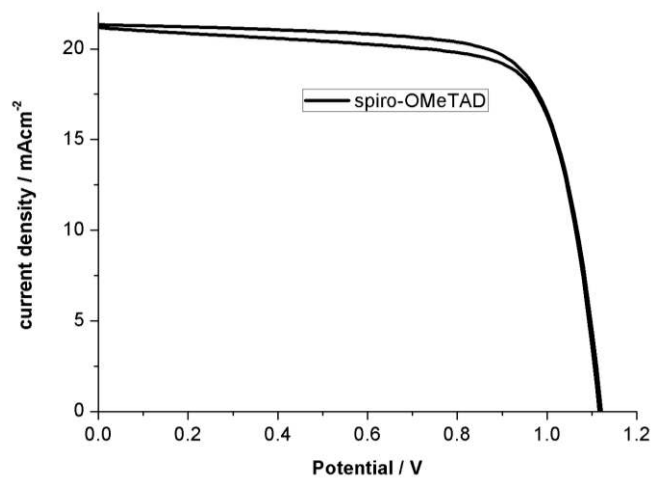
Figure S5.2.1. Hysteresis curve of the spiro-OMeTAD reference cell.
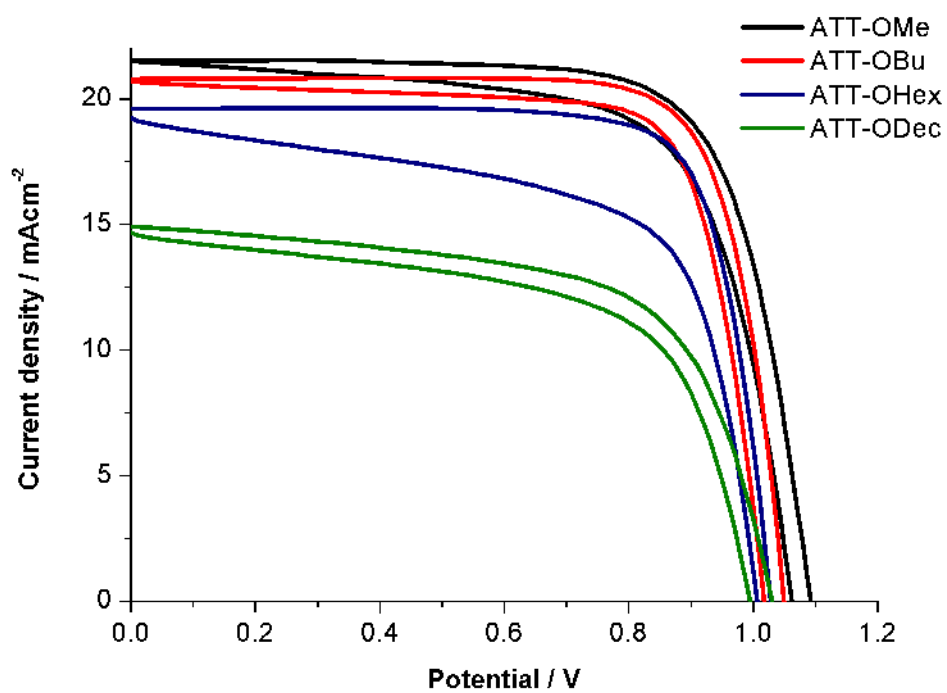
Figure S5.2.2. Hysteresis curves of the ATT derivatives measured at 20 mV/s.

5.3 Device statistics
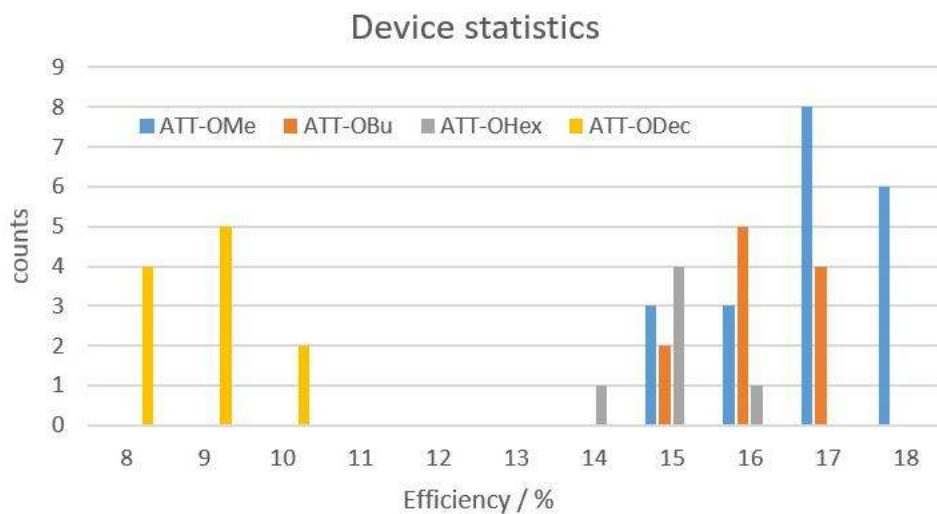
Figure 5.3.1. Efficiency distribution of devices fabricated using the different ATT derivatives.

5.4 Photoluminescence

Time-resolved PL experiments were performed with a spectrophotometer (Gilden Photonics) using a pulsed source at 460 nm (Ps diode lasers BDS-SM, pulse with < 100 ps, from Photonic Solutions, approx. 1 mW power, 20 MHz repetition rate, approx. 500 um spot radius) and the signal was recorded at 780 nm by the Time Correlated Single Photon Counting detection technique with a time resolution of 1 ns. The glass/perovskite/HTM samples were excited from the HTM side under ambient conditions. All the samples have been encapsulated in inert atmosphere to prevent any sample degradation or influence of moisture and oxygen. Monoexponential and bi-exponential fittings were used to analyze the background-corrected PL decay signal.

6. Supplementary figures

6.1. DSC
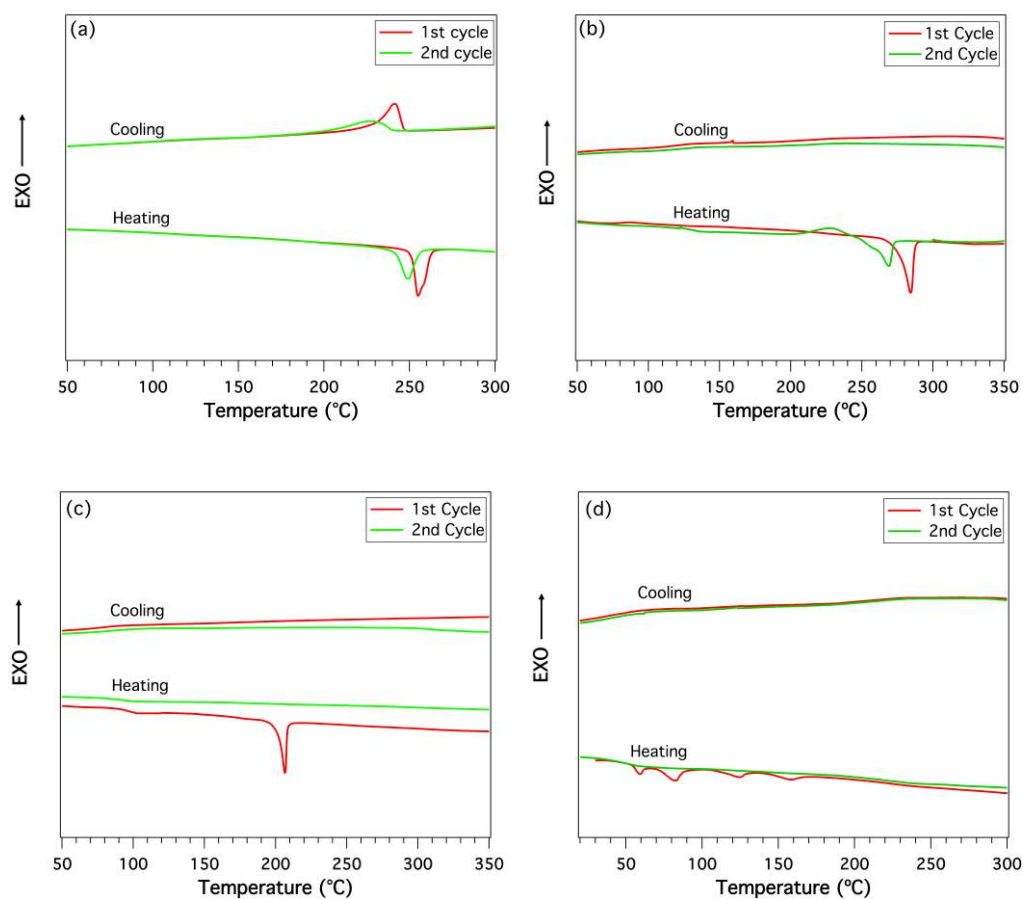
Figure S6.1.1. DSC of ATT-OMe (a), ATT-OBu (b), ATT-OHex (c) and ATT-ODec (d) at scan rate of 20 °C/min.

6.2 NMR, MS
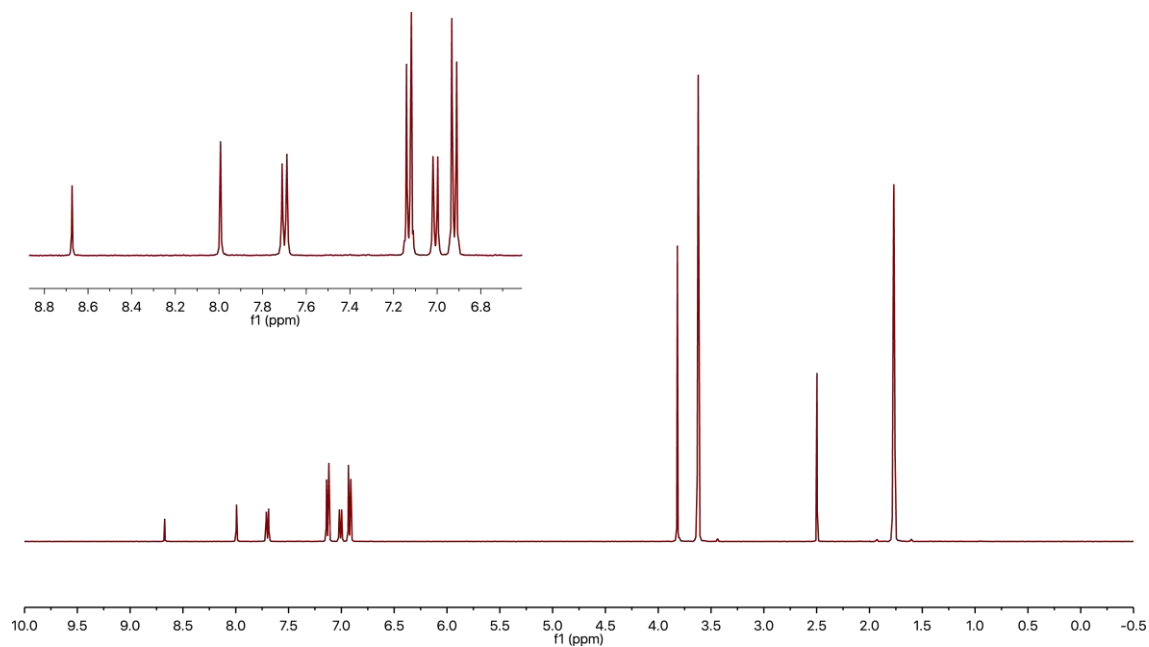
Figure S6.2.1.^{1}H NMR (400 MHz, THF-d8, 298 K) of compound ATT-OMe.
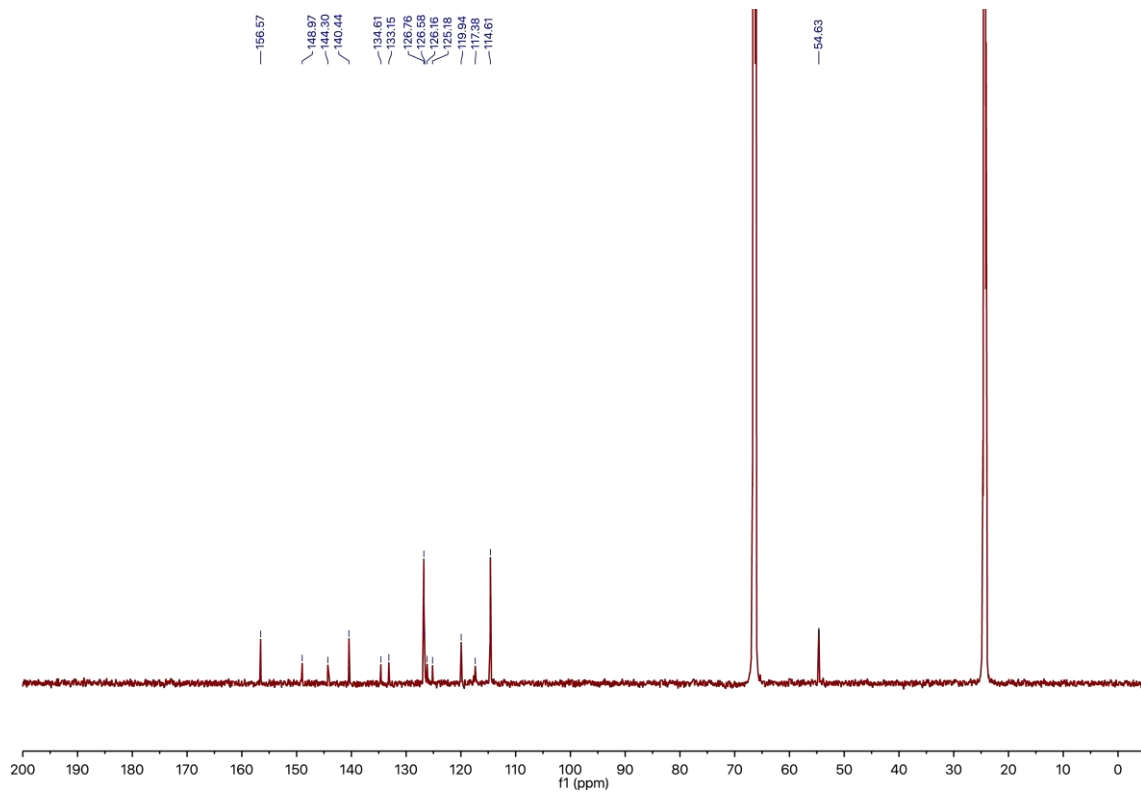
Figure S6.2.2.^{13}C NMR (176 MHz, THF-d8, 298 K) of compound ATT-OMe.

40
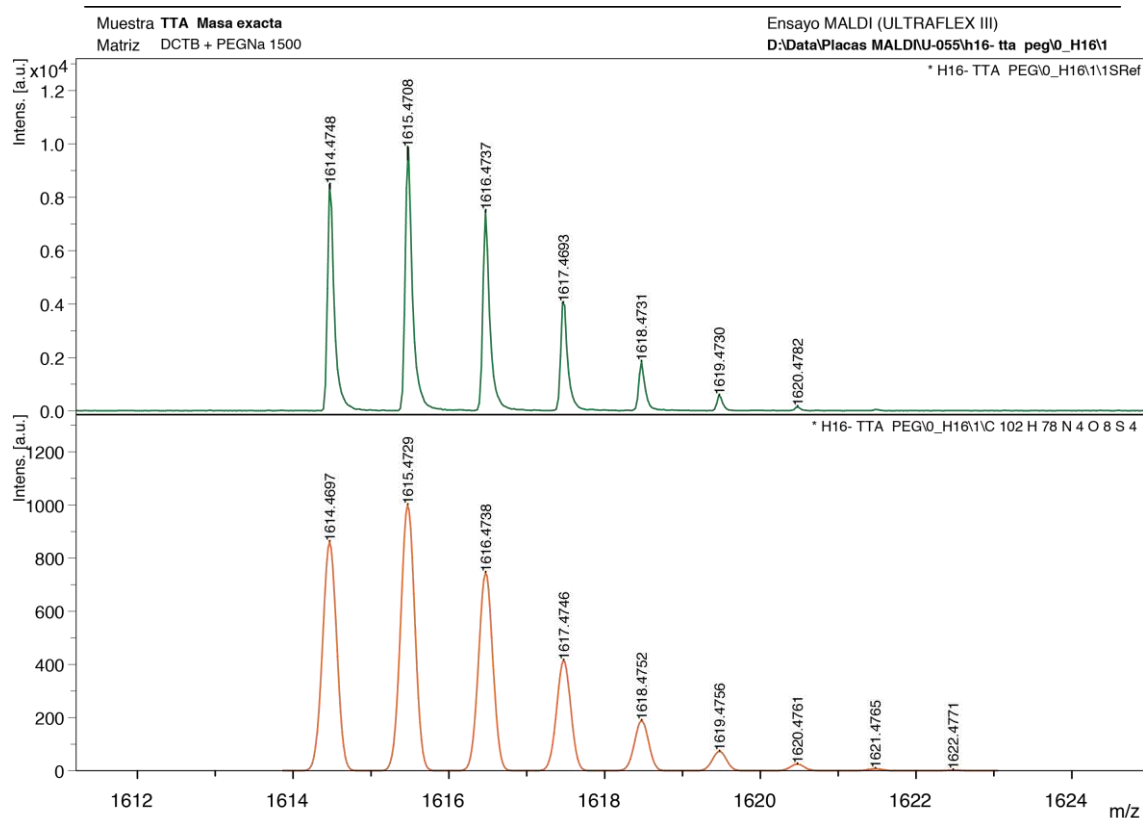
Figure S6.2.3. MALDI-TOF mass spectrum of ATT-OMe.
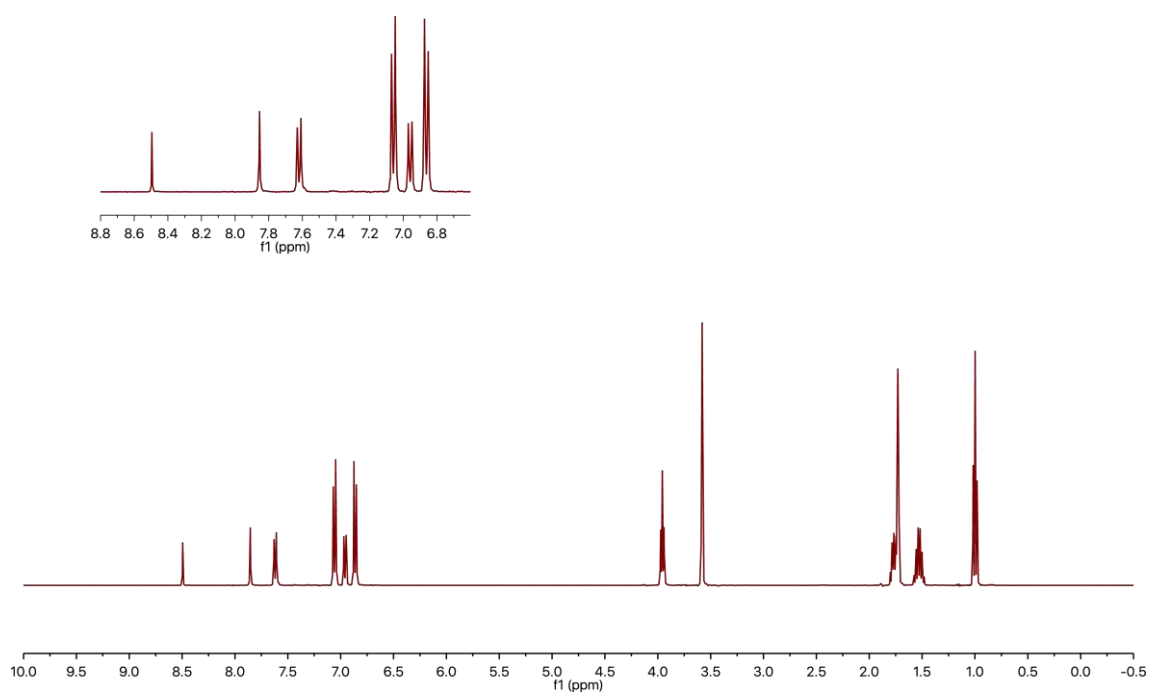
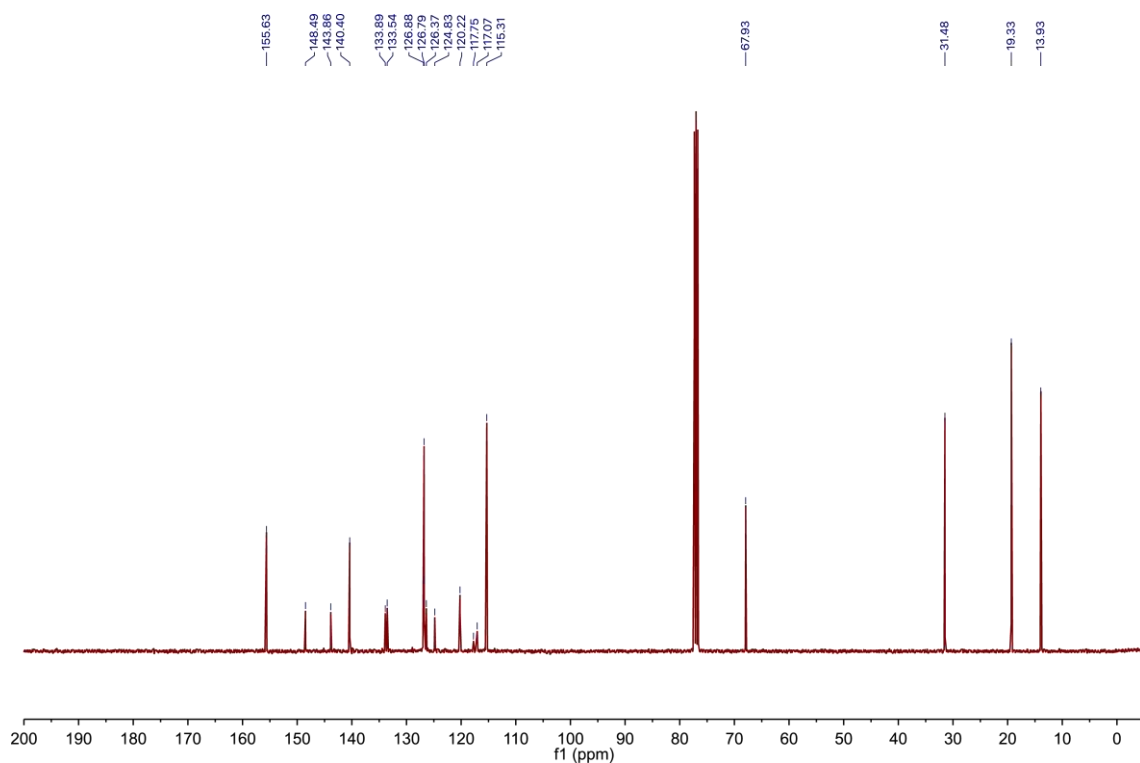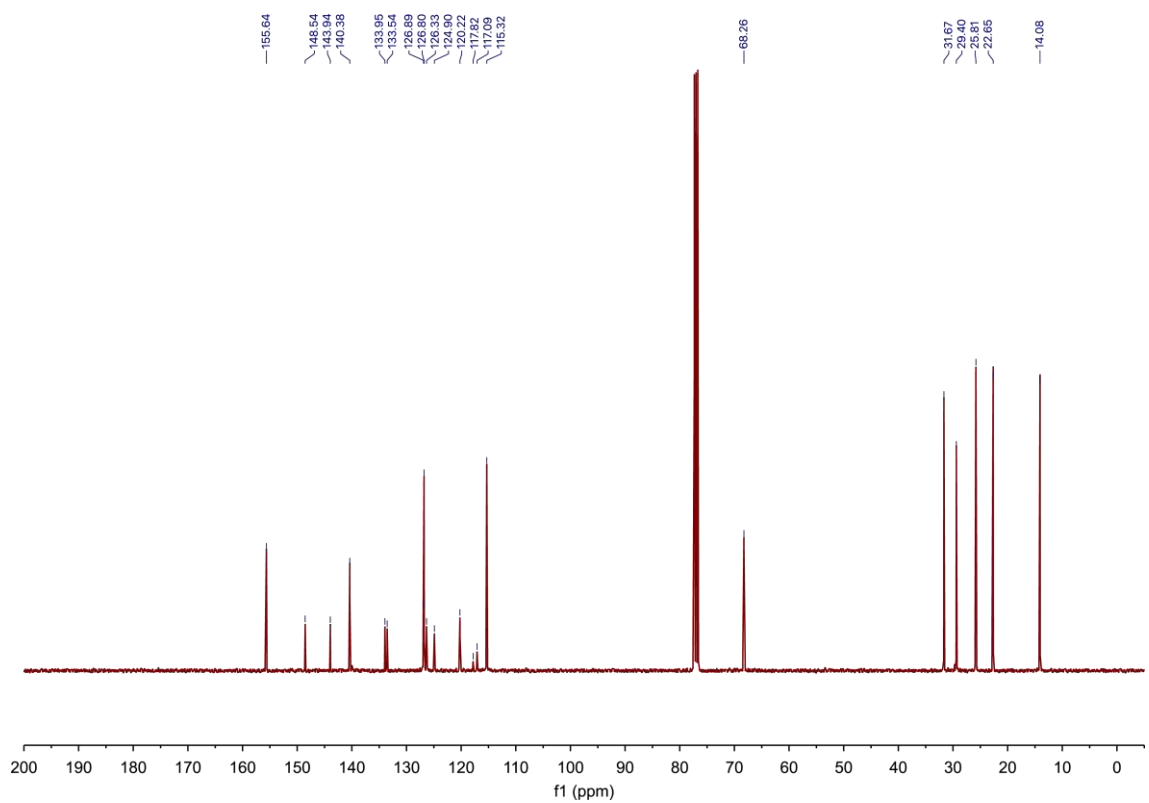**Figure S6.2.4.** ^{1}H NMR (400 MHz, THF-d8, 298 K) of compound ATT-OBu.

41

Figure S6.2.5.^{13}C NMR (100 MHz, CDCl$_3$, 298 K) of compound ATT-OBu.
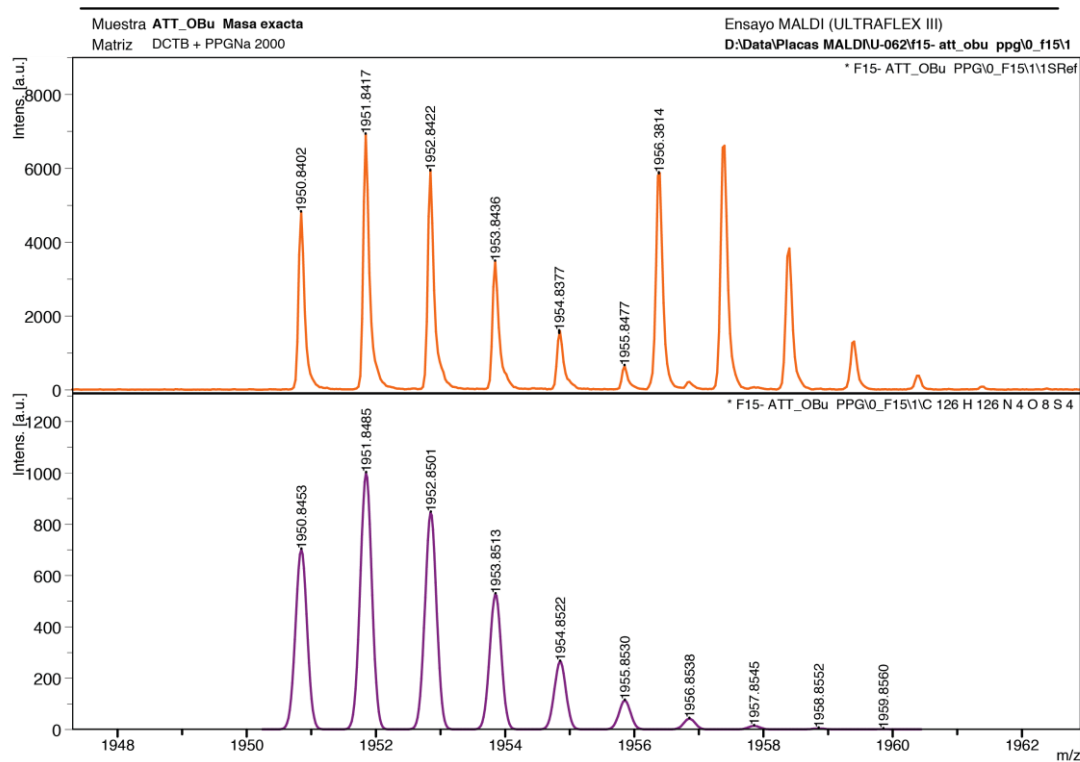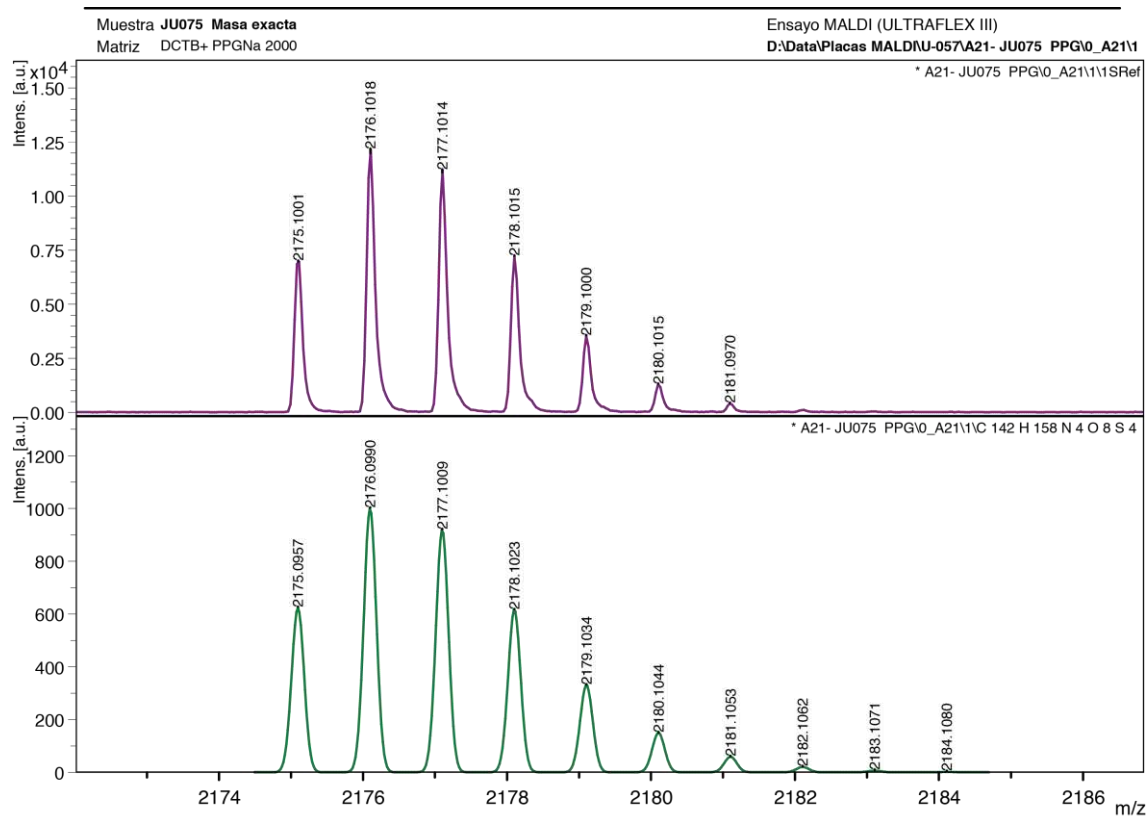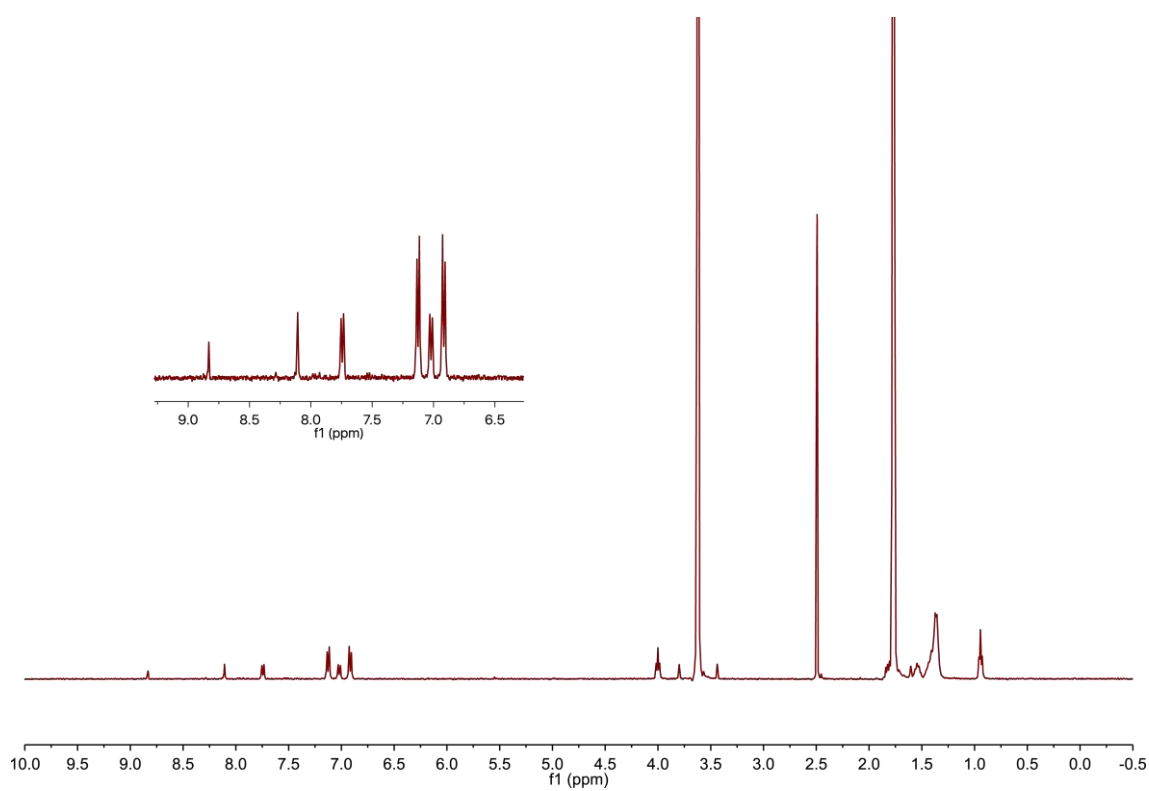

Figure S6.2.6.MALDI-TOF mass spectrum of ATT-OBu**.**
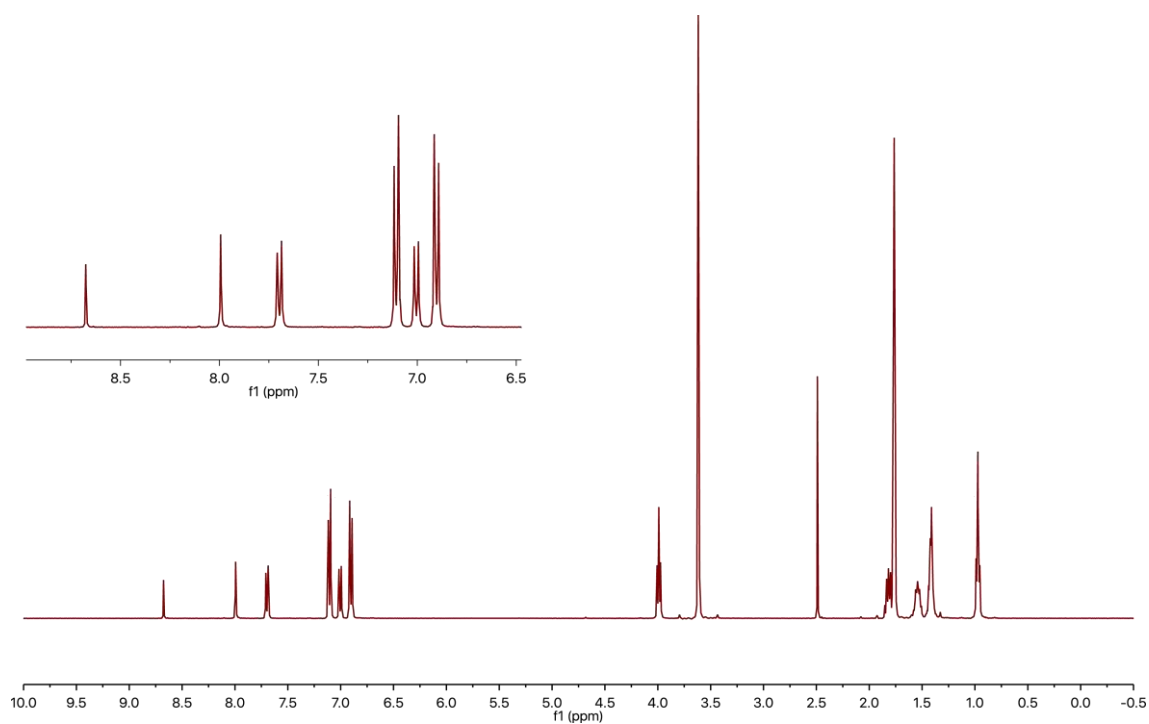
Figure S6.2.7.^{1}H NMR (400 MHz, THF-d8, 298 K) of compound ATT-OHex.

Figure S6.2.8.^{13}C NMR (100 MHz, CDCl$_3$, 298 K) of compound ATT-OHex.

43

Muestra **JU075 Masa exacta**
Matriz   DCTB+ PPGNa 2000

Ensayo MALDI (ULTRAFLEX III)
D:\Data\Placas MALDI\U-057\A21- JU075 PPG\0_A21\1

Figure S6.2.9. MALDI-TOF mass spectrum of ATT-OHex**.**

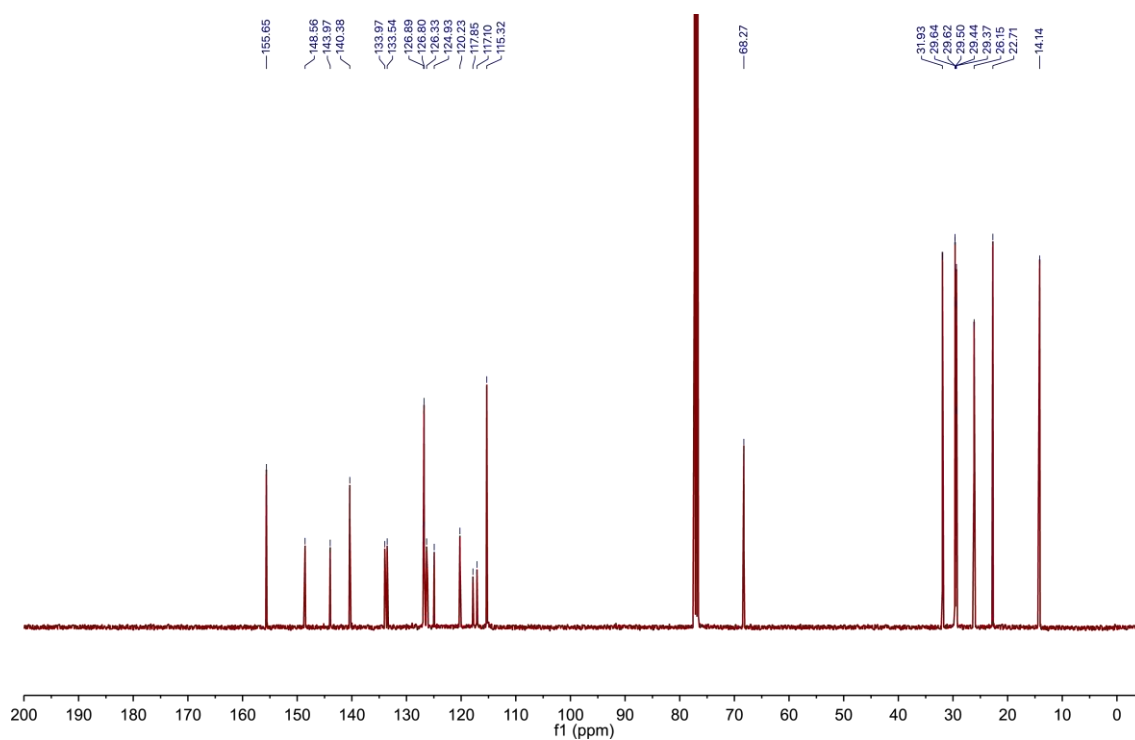**Figure S6.2.10.** ^{1}H NMR (400 MHz, THF-d8, 298 K) of compound ATT-ODec.

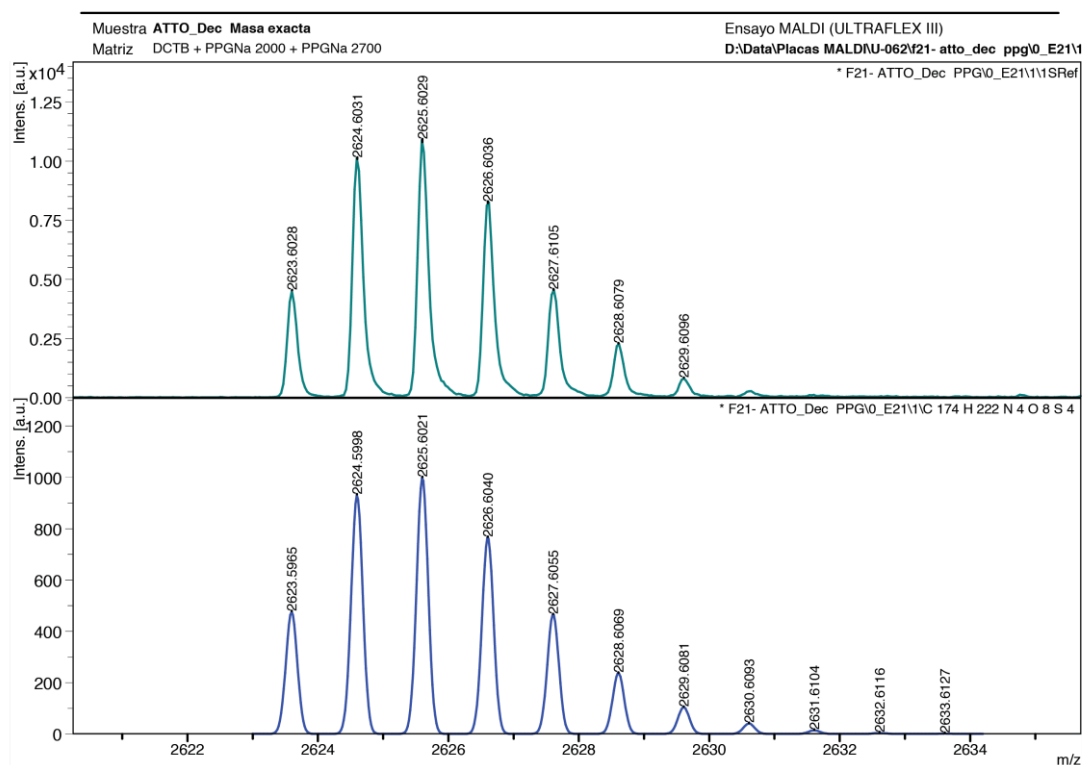**Figure S6.2.11.** ^{13}C NMR (100 MHz, CDCl$_3$, 298 K) of compound ATT-ODec.

Figure S6.2.12. MALDI-TOF mass spectrum of ATT-ODec.
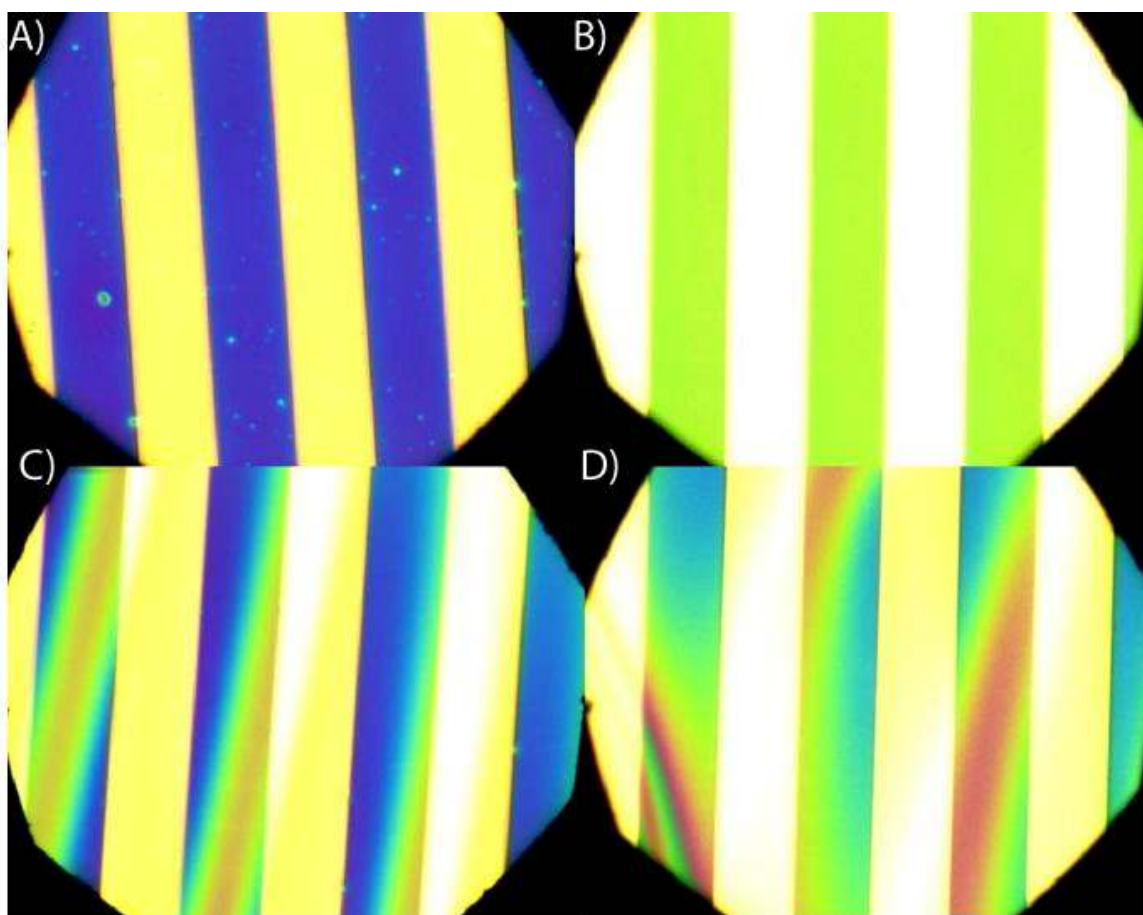
45

6.3 HTM layers

Figure S 6.3.1. Optical microscope images of the different HTM layers on substrates used for the conductivity measurement. Channel length is 20 μm. A) ATT-OMe, B) ATT-OBu, C) ATT-OHex, D) ATT-ODec.